COMPLEX-ENERGY DESCRIPTION OF MOLECULAR AND NUCLEAR OPEN QUANTUM SYSTESMS

By

Xingze Mao

A DISSERTATION

Submited to
Michigan State University
in partial fulfillment of the requirements
for the degree of

Physics – Doctor of Philosophy
Computation Mathematics, Science and Engineering - Dual Major

2020

ABSTRACT

COMPLEX-ENERGY DESCRIPTION OF NUCLEAR AND ATOMIC OPEN QUANTUM SYSTESMS

Xingze Mao

Quantum systems lying close to the decay threshold experience coupling to the scattering environment, hence they belong to a class of open quantum systems (OQSs). The study of OQSs requires proper treatment of non-localized scattering states and resonances. The Gamow shell model (GSM), as an extension of the traditional shell model formulated in the complex-momentum (k) plane, can properly treat the structural and decay properties of these threshold systems by employing the Berggren ensemble as the single-particle (s.p.) basis. In this thesis, GSM has been used to study two types of OQSs: (i) atomic systems such as quadrupolar anions and anions bounded by a multipolar Gaussian potential; and (ii) light nuclei, such as lithium isotopes and their mirror partners. In atomic systems, low-ℓ channels are found to be essential in defining the trajectories of resonant states near the dissociation threshold. In nuclear systems, a finite-range interaction has been optimized to give a realistic description of the spectra, ranging from well-bound systems to unbound nuclei above the decay threshold.

This dissertation is dedicated to my parents

ACKNOWLEDGEMENTS

I would first like to thank my advisor Witold Nazarewicz for all his support and insightful guidance, especially for his patience to correct all my errors and the freedom I was given to try all my ideas when things do not go well. The principle he told me to challenge myself every day and the high standard he held doing research will push me further in my career. It's been a great honor to finish my Ph.D. thesis under the guidance of Witold Nazarewicz. Great thanks to my Ph.D. committee members, Filomena Nunes, Morten Hjorth-Jensen, Brian O'Shea, Metin Aktulga, and Hironori Iwasaki, for the awesome guidance and cheering me up during all my committee meetings with all the great questions.

A big thanks to Kévin Fossez, Jimmy Rotureau, Simin Wang, Nicolas Michel, Yannen Jaganathen, and Erik Olsen for their support, scientifically and technically. They have been of great help to my research and are always ready to put aside things in their hands to help me whenever I brought up any questions to them. It would be way more difficult for me to finish my research without the help from you guys. Useful discussions with Marek Płoszajczak and Rodolfo Id Betan are also acknowledged.

I will regret if I did not mention all the smart and energetic geniuses I met along my way, Dan Liu, Hao Lin, Zachery Matheson, Terri Poxon-Pearson, John Bower, Thomas Redpath, Timofey Golubev, Tenzin Rubga, Bakul Agarwal, Chunli Zhang, Maxwell Cao, Mengzhi Chen, Tong Li, Xueying Huyan, Didi Luo, Zachary Constan. It was a great pleasure to work with you all on coursework, projects and non-scientific activities.

Thank you all for the accompany during this journey. This is an invaluable asset to my life. Special thanks to Simin and Josh for helping me debug this thesis.

I would also like to express my gratitude to Kim Crosslan, Scott Pratt, Artemis Spyrou, and Hironori Iwasaki for their support. Thank you for making this journey easier.

I was so lucky to join the MSU taekwondo and judo team and to train with all the wonderful fellows. Besides all the physical and mental improvements, I also learned a lot from Ron's martial philosophy and Sheehan's candidness, especially when he shouted "Mao, your throw is disgusting". I would also like to express my gratitude to all my training mates, Sarah, Kimberly, Neil, Soojin, Sam, Vici, Andrew, Igor, Jiayi, Susan, Schukou, Davina, Smiley, Joshua, Hainite, Jun, Patrick, Alfonso, John, Pablo, James. Thank you all and it was a good time training with you in the dojang.

Finally, I would like to express my love and gratitude to my family. I am so grateful for the love and support of my parents. Thanks for being there with me during all the ups and downs. I am also very lucky and fortunate to be embraced by the love and support of my wife Huan. I would also like to thank my sister for everything, especially for saving me my favorite snacks when I traveled back home, even though we fought a lot growing up. Love you all.

Contents

List of Figures . . . . **viii**

List of Tables . . . . **xiv**

1 Introduction **1**

1.1 Open quantum systems 1

1.1.1 Atomic systems 2

1.1.2 Nuclear systems 3

1.2 Outline 4

2 Berggren ensemble **5**

2.1 Gamow states 5

2.2 Antibound states 6

2.3 Berggren completeness relation 7

3 Atomic anions **10**

3.1 Electron-plus-molecule Model 12

3.1.1 Model and Hamiltonian 12

3.1.2 Coupled-channel equations 14

3.2 Results for quadrupolar anions 16

3.2.1 Critical quadrupolar moments 16

3.2.2 Rotational bands in the continuum 19

3.3 Results for anions bounded by multipolar Gaussian potentials 21

3.3.1 Threshold trajectories for multipolar Gaussian potentials in the adiabatic limit 23

3.3.2 Resonances of the near-critical quadrupolar Gaussian potential 25

3.3.3 Rotational motion 36

4 Lithium isotopes and mirror nuclei 41

4.1 Introduction 41

4.2 Gamow shell model 42

4.2.1 Hamiltonian 42

4.2.2 Interaction optimization 46

4.2.3 Model space 47

4.3 Results 49

4.3.1 Optimized states 49

4.3.2 Optimized Interaction 51

4.3.3 Test against other excited states 52

4.3.4 Root-mean-square radius 55

4.3.5 Prediction for unbound nuclei: ^{10}Li, ^{10}N and ^{11}O . . . 56

4.3.6 Continuum effects on the Thomas-Ehrman shift . . . 61

5 Conclusion and Outlook 64

6 List of Publications 66

List of Figures

2.1 S.p. states in the complex-momentum plane. Bound states (b) and antibound states (a) lie on the positive and negative imaginary-k axis, respectively. Capturing states (c) and decaying resonances (d) lie symmetrically in the third and fourth quadrants. The thick dashed line shows the deformed contour with antibound states included in the Berggren completeness relation. Taken from Ref. [1]. 8

3.1 A schematic illustration of the complex-energy electron-plus-molecule model used in this work. Taken from Ref. [2]. . . . 12

3.2 Critical prolate electric quadrupole moment as a function of the orbital angular momentum cutoff $\ell_{\max}$ in coupled-channel calculations in the adiabatic limit ($I \rightarrow \infty$) The internuclear distance is fixed at $s = 1.6\,a_0$ and the corresponding value of $Q^{+}_{zz,c} = 6.372016\,ea_0^2$ is indicated by the dotted line. The DIM results are marked by stars. The DIM result from [3] is denoted by a square at $\ell_{\max} = 10$. The convergence of the BEM results with respect to the momentum cutoff is shown for $k_{\max} =$ 6,8,10,and $12\,a_0^{-1}$. Taken from Ref. [4]. 18

3.3 Yrast band of quadrupolar anions defined by an internuclear distance of $s = 1.6\,a_0$, a moment of inertia of $I = 10^4\,m_e a_0^2$, and quadrupole moments of Q^-_{zz}=$-2.42\,ea_0^2$ and Q^+_{zz}=$+6.88\,ea_0^2$ on panels (a) and (b), respectively. The BEM and DIM results are denoted with empty circles and stars, respectively, and are almost indistinguishable for all orbital angular momentum cutoffs considered. Taken from Ref. [4]. 21

3.4 Threshold trajectories $(V_0, r_0)^\pm_c$ for multipolar Gaussian potentials with $\lambda = 1 - 4$ in the adiabatic limit. Taken from Ref. [2]. 23

3.5 The lowest 0^+ resonant state of the quadrupolar Gaussian potential with $r_0 = a_0$ as a function of V_0. Top: real energy and imaginary momentum. Bottom: the channel decomposition of the real part of the norm. The critical strength $V_{0,c}$ is marked by arrow. Taken from Ref. [2]. 26

3.6 Trajectory of the 0^+ resonant state in the complex-k plane of the quadrupolar potential with $r_0 = 4\,a_0$ as the potential strength V_0 increases in the direction indicated by an arrow. At the lowest value V_0 =1.1 Ry, the 0^+ g.s. is bound and the state of interest is an excited 0^+_2 state associated with a decaying resonance. At $V_0 = 1.8$ Ry the pole crosses the $-45°$ line and becomes a subthreshold resonance 0^+_d. At $V_0 = 2.857$ Ry the decaying pole reaches the imaginary-k axis and coalesces with the capturing pole with $\mathrm{Im}(k) < 0$ forming an exceptional point. The antibound states at $V_0 = 1.8$ Ry and $V_0 = 2.7$ Ry are marked. Taken from Ref. [2]. 28

3.7 Real norms of the channel wave functions for the decaying pole 0^+_d shown in Fig. 3.6 and the antibound states 0^+_b and 0^+_c of Fig. 3.8. Taken from Ref. [2]. 29

3.8 Trajectories of antibound and bound 0^+ states along the imaginary-k axis as a function of V_0 for the quadrupolar potential with $r_0 = 4\,a_0$. With increasing potential strength, the antibound states 0^+_a, 0^+_b, and 0^+_c become bound states of the system 0^+_1, 0^+_2, and 0^+_3, respectively. The open circle marks the exceptional point of Fig. 3.6, which is the source of two antibound states. The particular values of V_0 discussed around Fig. 3.6 are marked. Taken from Ref. [2]. 31

3.9 Trajectory of the 0_d^+ resonant state in the complex-k plane for different values r_0 of quadrupolar potential as indicated by numbers (in units of a_0). The ranges of V_0 (in Ry) are: (25.6-29.0) for $r_0 = a_0$; (9.7-14.5) for $r_0 = 1.5\,a_0$; (4.8-10) for $r_0 = 2\,a_0$; (1.7-4.79) for $r_0 = 3\,a_0$; and (1.1-2.85) for $r_0 = 4\,a_0$. Taken from Ref. [2]. 32

3.10 Top: trajectory of the lowest 1_1^- resonant state of the quadrupolar potential with $r_0 = a_0$ as a function of V_0 in the range of (9-12.7) Ry. The potential strength V_0 increases along the direction indicated by an arrow. The positions of the bound and antibound states at $V_0 = 12.34\,\mathrm{Ry}$ and $12.4\,\mathrm{Ry}$ are marked. Bottom: real norms of channel functions for this state. Taken from Ref. [2]. 34

3.11 The rotational band built upon the $J^\pi = 0_1^+$ state of a dipole-bound anion. The parameters $V_0 = 5.33\,\mathrm{Ry}$, $r_0 = a_0$, and $I = 10^3\,m_e a_0^2$ have been chosen to place the bandhead energy slightly below the zero-energy threshold, where the rotational motion of the molecule can excite the system into the continuum. The energy is plotted as a function of $J(J+1)$. Taken from Ref. [2]. 36

3.12 Similar to Fig. 3.11 but for rotational bands built upon the $J^\pi = 0_1^+$ and 1_1^- bandheads of a quadrupolar Gaussian potential with $V_0 = 12.38\,\mathrm{Ry}$, $r_0 = a_0$, and for $I = 50\,m_e a_0^2$ and $I = 100\,m_e a_0^2$. Taken from Ref. [2]. 37

3.13 Energy (a) and decay width (b), both in Ry, of the 3_1^- resonance of the quadrupolar Gaussian potential with $r_0 = a_0$ as a function of the inverse of the moment of inertia and the potential strength. The dissociation threshold ($E = 0$) is indicated. The dominant (j, ℓ) channel is marked in panel (b). When the rotational energy of the molecule $E_{\text{rot}}^{j=4}$ lies below/above the energy of the 3_1^- resonance, the (4,1) decay channel is open/closed. The line $E_{\text{rot}}^{j=4} = E(3_1^-)$ (thick solid) separating these two regimes is marked, so is the line $E_{\text{rot}}^{j=2} = E(3_1^-)$ (thick dotted) which corresponds to the threshold energy for the opening of the (2,1) channel. The norms of the two dominant channels (2,1) (solid line) and (4,1) (dotted line) are shown as a function of V_0 for $1/I = 0.04\, m_e^{-1} a_0^{-2}$ (c) and $0.02\, m_e^{-1} a_0^{-2}$ (d). Taken from Ref. [2]. 39

4.1 Energies for states of Li isotopes with respect to ^{4}He. Red lines denote GSM results and the black lines mark experimental values. The shaded area represents the width of the corresponding resonance. States used for optimization are marked with a ★, their energies are listed in Tables 4.1 and 4.5. 53

4.2 Similar to Fig. 4.1 for results of mirror nuclei of Li isotopes. Experimental energy of the $5/2^-$ resonance in ^{9}C was taken from Ref. [5] and the data for ^{11}O is from Ref. [6]. 57

4.3 Spectrum for Li isotopes and their mirror partner with mass (a) $A = 7$, (b) $A = 8$, (c) $A = 9$, (d) $A = 10$. Within each pair, the spectrum of Li isotope and its mirror are plotted whin the same scale and different range. The plots are shifted so that the g.s. of each pair align with each other. The one-proton/neutron emission thresholds are also marked within each plot. 62

List of Tables

4.1 Energy levels used in the GSM Hamiltonian optimization. The energies are given with respect to the ^{4}He g.s.. The experimental values E_{exp} are taken from Ref. [7]. They are compared to the GSM values E_{GSM}. 50

4.2 Central and spin-orbit strengths of the core-nucleon WS potential optimized in this work. The statistical uncertainties are given in parentheses. 51

4.3 Groud state energies (in MeV) and widths (in keV) of ^{5}He and ^{5}Li obtained from the optimized core-nucleon potential and compared to experiments [8, 9]. 51

4.4 Strengths V_η^{ST} of the two-body interaction optimized in this work. The statistical uncertainties are given in parentheses. 52

4.5 Energy levels for states not entering the optimization. The experimental values E_{exp} are taken from Ref. [7]. The GSM values E_{GSM} are shown with the uncertainties in parentheses. 54

4.6 Root-mean-square proton (R$_p$) and neutron (R$_n$) radii of ^{6}Li, ^{7}Li/^{7}Be, ^{8}Li/^{8}B, ^{9}Li/^{9}C, and ^{11}Li (in fm). 55

4.7 Squared amplitudes of dominant configuration of valence neutrons and protons for low-lying levels of ^{10}Li and ^{10}N, respectively. The odd proton in ^{10}Li and the odd neutron in ^{10}N occupy the $0p_{3/2}$ Gamow state. The tilde sign labels non-resonant continuum components. 59

Chapter 1

Introduction

1.1 Open quantum systems

Due to their weakly bound/unbound nature, OQSs are strongly affected by the environment. There are many examples of OQSs across different physics areas, such as nuclear physics, atomic and molecular physics, quantum optics, microwave resonators, and nanoscience. Despite some distinct features, these OQSs share many generic properties related to the presence of resonant states, exceptional points, threshold behavior, etc.

Most isotopes far away from the beta-stability line fall into the category of OQSs. Moreover, even for those well-bound isotopes, the continuum coupling should not be overlooked when considering excited states near the particle decay threshold. Studies on such exotic systems offer unique opportunities to test theory, as well as understanding the important features of continuum coupling in OQSs.

In order to describe continuum coupling properly, two problems need to be addressed. Firstly, in practice, one need to discretize the continuum states numerically, while ensuring the completeness of the s.p. basis. Consequently, in larger systems involving many-body correlations, computational work can become prohibitively expensive. Secondly, these unbound states, including decaying resonances, are not square-integrable. Accordingly, to describe OQSs, one needs to go beyond the standard Hilbert-space quantum mechanics which deals with L^2-integrable states.

This raises a challenge for the theoretical studies. One way to deal with these problems is to extend the system Hamiltonian into the complex-energy (or momentum) plane with the Berggren basis [10]. Since the Berggren ensemble includes bound states, decaying resonances, and non-resonant scattering states, the continuum effect can be taken into account properly. Based on this, several approaches, such as complex-energy electron-plus-molecule model and GSM have been developed. In this work, we use these approaches to study molecular and nuclear OQSs.

1.1.1 Atomic systems

In atomic physics, anions are neutral molecules that can attach an excess electron. This valence electron is bounded by the weak Coulomb potential of the molecule due to electrostatic polarization effects, which makes anions good candidates to study physics questions pertaining to OQSs.

Anions are difficult to identify experimentally, due to the high order polarization as well as the weakly bound/unbound property. Therefore, to provide some guides for the experimental study, we used a complex-energy electron-plus-molecule model to analyze the behavior of polarized anions, where both electron motion and molecular rotational motion are considered and coupled. In particular, the properties of quadrupolar anions and the molecular anions bounded by the multipolar Gaussian are discussed in Chapter 3.

1.1.2 Nuclear systems

In low-energy nuclear physics, the development of next-generation experimental facilities (including FRIB at Michigan State University) will allow more rare isotopes, which inhabit remote regions of the nuclear landscape, to become accessible [11]. Properties of these isotopes are at the forefront of nuclear structure and reaction research, which provide unique opportunities to study OQS phenomena. In threshold regions around particle drip lines strong continuum coupling effect are present, which result in exotic nuclear properties such as nuclear halos [12, 13, 14], presence of unexpected intruder states [15, 16, 17], clusterization [18, 19], appearance of new 'magic' numbers, and two-nucleon decay [20, 21, 22, 23].

In this thesis, we are interested in halo systems, in which the valence nucleons are impacted by the continuum environment. The halo phenomenon was first discovered in ^{11}Li [24]. Another example is ^{11}Be, where continuum effects play a significant role in forming the halo structure as well as the inversion of the ground state (g.s.) parity [25, 26, 27, 28].

Halo systems are often studied within phenomenological models, which assume the presence of large cluster substructures [29, 17]. In this work, we use the GSM to reveal how weakly bound (or unbound) nuclear states are formed and affected by many-body correlations. Specifically, the lithium isotopes and their mirror partners have been studied with an effective Hamiltonian optimized to selected low-lying nuclear states. These results will be discussed in Chapter 4.

1.2 Outline

This thesis is on the application of a complex-energy configuration interaction approach to the nuclear and atomic OQSs. In Chapter 2, a complex-momentum Berggren basis is introduced. Chapter 3 presents the work on atomic anions, including both quadrupolar anions and anions bound by multipolar Gaussian potentials. In Chapter 4, we study the lithium isotopes and their mirror partners. Finally, this thesis concludes in Chapter 5 with a summary of our results and an outlook for future studies.

Chapter 2

Berggren ensemble

In well-bound systems, which can be viewed as closed quantum systems, the wave functions of the low-lying states are spatially localized and can thus be expanded in the harmonic oscillator (HO) basis, which decays asymptotically. In OQSs, however, coupling to the environment becomes non-negligible and non-localized continuum states must be considered. An approach that goes beyond the Hilbert space is needed. In our work, we use a more general basis, named Berggren basis [10], to study OQSs.

In this chapter, Gamow states, being one of the most important features in OQSs, will be first introduced. Berggren completeness relation, used in all the calculations through this thesis, is then illustrated.

2.1 Gamow states

Gamow states [30, 31], also known as resonant or Siegert [32] states, were introduced for the first time by George Gamow in 1928 to describe the phenomenon of α decay. In the quasi-stationary formalism, Gamow states have complex energy:

$$\tilde{E}_n = E_n - i\frac{\Gamma_n}{2}, \tag{2.1}$$

where the real part E_n corresponds to the mean energy of the state and the imaginary part can be associated with the decay width Γ_n. The decay width is related to the decay half-life by the usual relation:

$$T_{1/2} = \frac{\hbar \mathrm{ln} 2}{\Gamma}. \tag{2.2}$$

Similar to bound states, resonances are poles of the scattering matrix in the complex-momentum plane, reflecting the properties of binding potential. In the complex-momentum plane, bound states lie on the positive imaginary-k axis $k_n = -i\kappa_n$ ($\kappa_n > 0$), while decaying resonances lie in the fourth quadrant with $k_n = \kappa_n - i\gamma_n$ ($\kappa_n > 0, \gamma_n > 0$), as shown in Fig. 2.1. Capturing resonances are located symmetrically in the third quadrant. Decaying resonances with $\kappa_n < \gamma_n$ are referred to as subthreshold resonances [33, 34, 35, 36]. While they can not be observed experimentally, their presence impacts the inner structure as well as the corresponding observables. Although the positive-energy Gamow states are not square-integrable in real space, they can still be normalized through complex-scaling method [37, 38] by choosing a proper integration path in the complex plane.

2.2 Antibound states

Antibound states [39, 40, 41, 42], also known as virtual states, lie in the negative imaginary axis of the complex-momentum plane with $k_n =$

$-i\kappa_n(\kappa_n > 0)$. With real and negative energy similar to bound states, virtual states lie on the second Riemann sheet of the complex energy plane and their wave functions are not localized. The negative imaginary momentum leads to exponentially diverging wave function in the space, $u(r) \sim e^{\kappa_n r}$. A physical interpretation of antibound states is usually difficult as the exponential increasing wave function cannot support a state. Therefore, similar to subthreshold resonances, antibound states cannot be measured. However, antibound states can reveal themselves with increased cross section near the threshold [43, 44, 45, 46].

2.3 Berggren completeness relation

Berggren completeness relation [10] was first proposed in 1968 to include the continuum states in a complex-plane s.p. basis:

$$\sum_n u_n(E_n, r)u_n(E_n, r') + \int_{\mathcal{L}^+} u(E, r)u(E, r')dE = \delta(r - r'), \tag{2.3}$$

The discrete term u_n includes both bound states and decaying resonances. The second term consists of the non-resonant continuum states along an arbitrary scattering contour $\mathcal{L}^+$ surrounding the poles u_n.

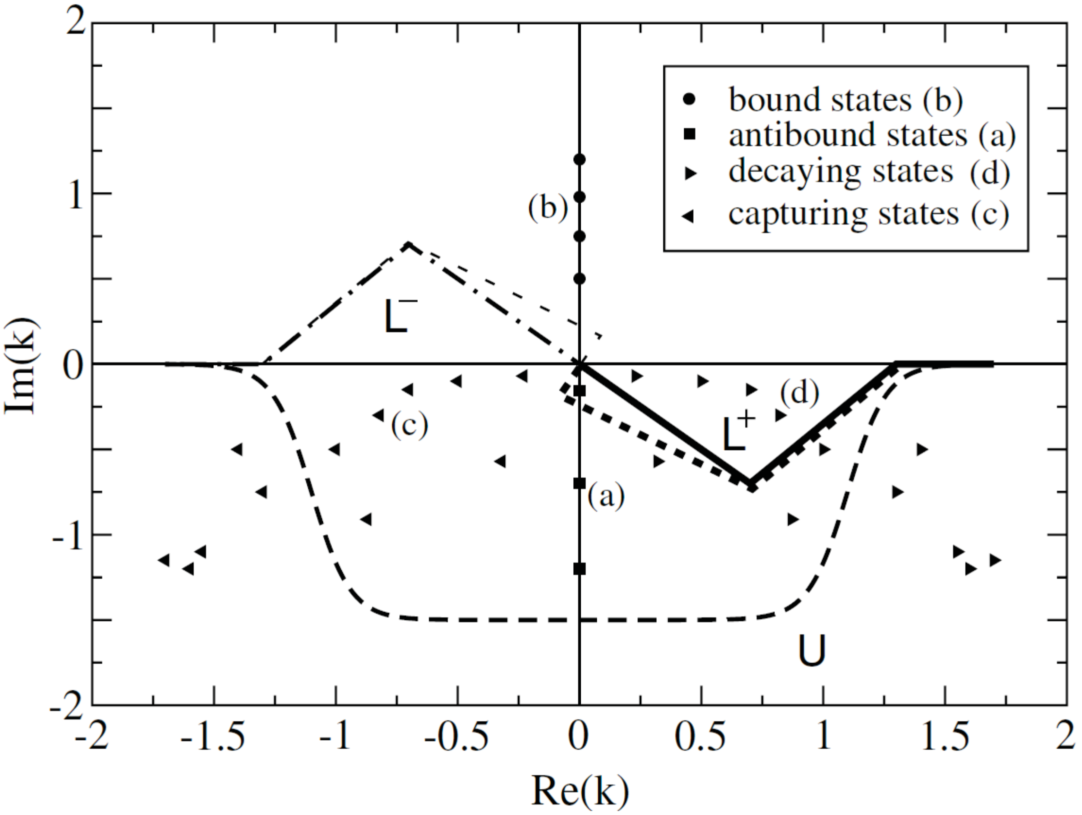

Figure 2.1: S.p. states in the complex-momentum plane. Bound states (b) and antibound states (a) lie on the positive and negative imaginary-k axis, respectively. Capturing states (c) and decaying resonances (d) lie symmetrically in the third and fourth quadrants. The thick dashed line shows the deformed contour with antibound states included in the Berggren completeness relation. Taken from Ref. [1].

The Berggren completeness relation for each partial wave can be seen more clearly in the momentum space:

$$\sum_{n\in(\mathrm{b,d})} |\tilde{u}_n\rangle \langle u_n| + \int_{\mathcal{L}^+} |u(k)\rangle \langle u(k)| \, dk = 1, \tag{2.4}$$

where b and d stands for bound states and decaying resonances, respectively. $\mathcal{L}^+$ is the scattering contour in complex-momentum plane. The tilde symbol indicates the time-reversal operation. As we show in Fig. 2.1, one can draw a contour $\mathcal{L}^+$ that starts from the origin, extends to the fourth quadrant, then comes back to the real axis and finally extends to the infinity along the real axis. As a result, the scattering states lying on the contour $\mathcal{L}^+$, bound states on the positive imaginary axis and the decaying resonances lying between the real axis and the contour $\mathcal{L}^+$ enter the Berggren completeness relation. Contours with different shapes are equivalent as long as all the resonant states between the real axis and the contour are included. Antibound states can also be included in the generalized completeness relations with slightly deformed contour $\mathcal{L}^+$. It is to be noted that in the unlikely situation that bound states of energies higher than antibound states are present, they must be excluded from the sum in Eq. (2.4), see Fig. 2.1.

In our applications, the contour $\mathcal{L}^+$ is defined by three points: k_{peak} in the fourth quadrant, k_{mid}, and cutoff momentum k_{max} on the real axis. The resulting three segments along the contour are usually discretized with (N_1,N_2,N_3) Gaussian-Legendre points. k_{max} and N need to be sufficiently large to ensure the completeness of the basis as well as the convergence of results. While the bound states are normalized in the standard way, decaying resonances are normalized using the exterior complex scaling method [37, 38]. The scattering states are normalized to the Dirac-delta function, (see Ref. [1]).

Chapter 3

Atomic anions

Since the critical moment μ_c required to bind an extra electron by a point-dipole was first determined by Fermi and Teller [47, 48, 49, 4], extensive theoretical as well as experimental studies [50, 51, 52, 53] have been carried out to investigate dipolar anions. However, this is not the case for other multipolar anions. As the higher-order multipolar potentials are even shallower than the dipolar potential, molecular anions associated with neutral cores with no dipole moments have been more challenging to find experimentally. One interesting question is to identify the limit of existence for higher-order multipolar anions. To determine the critical quadrupole moment needed to bind an excess electron, we carried out exploration of quadrupolar anions with a linear charge configuration.

The property of polarized anions above the dissociation threshold is also an interesting aspect to investigate. For example, the study of dipolar anions in Ref. [54] suggests the presence of different behavior in the strong-coupling (subthreshold) and weak-coupling (above threshold) regimes. One might wonder whether such a pattern would be present in quadrupolar anions, where the binding potential is more localized and deformed.

While the binding of multipole-bound anions is fragile, low-energy resonances in such systems are expected to be less sensitive to details of the short-range molecular potential as the spatial extension of the valence electron is huge. This situation resembles universal behavior, independent of the details of the interaction, exhibited by other weakly-bound/unbound quantum systems, such as nuclear halos, cold atomic gases near a Feshbach resonance, and helium dimers and trimers, see, e.g., Refs. [55, 56, 57, 58, 59, 60, 61, 62, 63, 64]. In all of those cases, simple arguments based on scale separation and effective field theory capture the essential physics [65, 66, 67, 68, 69, 70, 60]. However, due to the similarity of single-electron and rotational energy scales, coupling between the valence electron motion and molecular rotational motion might become complicated above the dissociation threshold [71, 72, 73, 74, 75, 76]. Therefore, to investigate generic properties of multipole-bound anions, in this work we include a nonadiabatic coupling between electronic and molecular motion in our complex-energy electron-plus-molecule model, and simulate the short-range multipole potential with a Gaussian form factor.

In this chapter, we present the framework of our complex-energy electron-plus-molecule model as well as the corresponding results for these two types of anions: (i) quadrupolar anions; and (ii) anions described by multipolar Gaussian potentials.

3.1 Electron-plus-molecule Model

3.1.1 Model and Hamiltonian

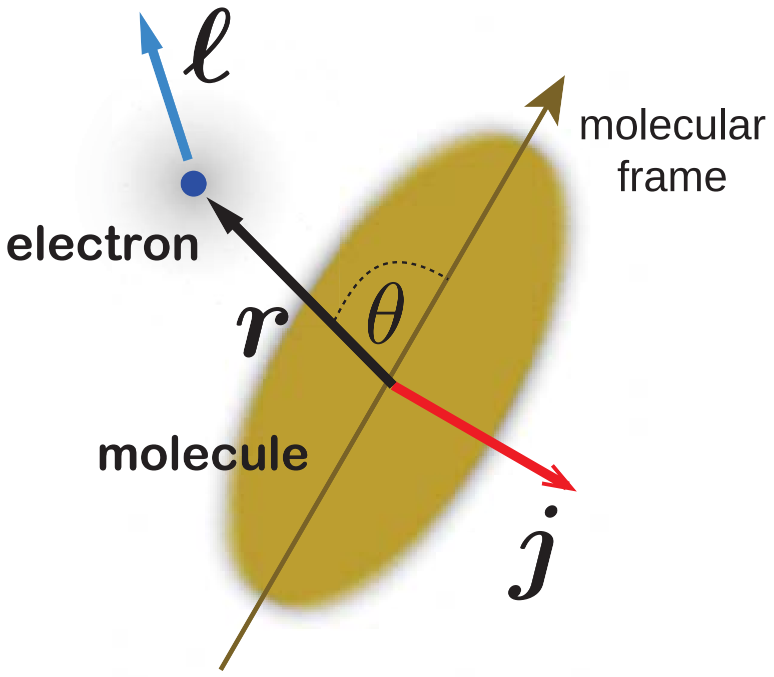

Figure 3.1: A schematic illustration of the complex-energy electron-plus-molecule model used in this work. Taken from Ref. [2].

As shown in Fig. 3.1, a polarized anion system can be schematically described as an electron moving in the potential generated by a multipole molecule. Neglecting the spin-orbit interaction and the vibrational motion of the molecule, the electron-plus-molecule Hamiltonian can be written as [77, 54]:

$$\hat{H} = \frac{\hat{j}^2}{2I} + \frac{\hat{p}_e^2}{2m_e} + V(\boldsymbol{r}). \tag{3.1}$$

The first term is the rotational energy of the molecule with angular momentum $\hat{j}$ and moment of inertia I. The second term represents the kinetic energy of the electron of mass m_e and linear momentum $\hat{p}_e$. $V(\boldsymbol{r})$

defines the effective interaction (potential) between valence electron and the molecule with $\boldsymbol{r}$ being the position vector pointing from the molecule to the valence particle.

Quadrupolar anion potential

To simulate the potential (electrostatic field) $V(\boldsymbol{r})$ in a quadrupolar anion, we consider a linear distribution of point charges (with the amount of charge q) separated by a distance of s. Two configurations of $(q, -2q, q)$ and $(-q, 2q, -q)$ correspond to a prolate and oblate shape, respectively, with the middle charge residing in the center of the molecule and $q > 0$. Considering the cylindrical symmetry along the molecule axis (z axis), a quadrupole moment of the considered configuration is $Q^{\pm}_{zz} = \pm 2qs^2$.

The potential $V(\boldsymbol{r})$ can be expressed through a multipole expansion:

$$V(r,\theta) = \sum_{\lambda} V_{\lambda}(r) P_{\lambda}(\cos\theta), \tag{3.2}$$

where $V_{\lambda}(r)$ is the radial part for each multipolarity λ. For the linear charge distribution $(\pm q, \mp 2q, \pm q)$ considered here, the form of $V_{\lambda}(r)$ can be explicitly written as:

$$V_{\lambda}(r) = \frac{e}{4\pi\epsilon_0}\frac{Q^{\pm}}{s^2}\begin{cases} \frac{1}{r_>} - \frac{1}{r} & \text{for } \lambda = 0, \\ (\frac{r_<}{r_>})^{\lambda}\frac{1}{r_>} & \text{for } \lambda = 2, 4, 6... \end{cases} \tag{3.3}$$

with $r_>$=max(r, s) and $r_<$=min(r, s). The angular part of the potential $P_{\lambda}(\cos\theta)$ is given by a Legendre polynomial of order λ, with θ being the angle between the direction of the valence electron $\boldsymbol{r}$ and the symmetry axis of the molecule, see Fig. 3.1.

Multipolar Gaussian potential

In multipolar Gaussian anions, the interaction between the molecule and the valence electron $V(\boldsymbol{r})$ can be modeled by a short-range potential of the axially-deformed Gaussian form with multipolarity λ:

$$V(\boldsymbol{r}) = -V_0 \exp\left(-\frac{r^2}{2r_0^2}\right) P_\lambda(\cos\theta), \tag{3.4}$$

where V_0 is the potential strength, and r_0 is the potential range.

3.1.2 Coupled-channel equations

The total angular momentum of the system $\hat{J}$ is given by the sum of the angular momenta of the molecule $\hat{j}$ and the valence electron $\hat{\ell}$. Although the potential $V(\boldsymbol{r})$ is deformed in the intrinsic frame, the whole system (electron + molecule) is rotationally invariant in the laboratory reference frame. Therefore, $\hat{J}$ commutes with the Hamiltonian $\hat{H}$ and the wave function can be written as:

$$\Psi^J = \sum_c u_c^J(r)\Theta_c^J, \tag{3.5}$$

where c labels all possible channels (j, ℓ) for a given J, $u_c^J(r)$ is the radial channel wave function, and Θ_c^J is the angular channel wave function. The eigenstates Eq. (3.5) are also labeled by means of the parity quantum number π; hence, in the following we use the spectroscopic notation J_n^π, where $n = 1$ marks the lowest J^π-state, $n = 2$ – the next one, and so on.

To properly describe the nonadiabatic coupling between the electronic and molecular motion, we solve the coupled-channel equations:

$$\left[\frac{d^2}{dr^2} - \frac{j_c(j_c+1)}{I} - \frac{\ell_c(\ell_c+1)}{r^2} + E_J\right] u_c^J(r) = \sum_{c'} V_{cc'}^J(r) u_{c'}^J(r), \tag{3.6}$$

which are obtained by inserting the wave function (3.5) into the Schrödinger equation. $V_{cc'}^{J}(r)$ is the channel-channel coupling potential, and can be evaluated by rewriting the multipolar potential $V(\boldsymbol{r})$ in the laboratory frame [77, 54]. In this case, the motion of the electron is weakly coupled to the rotation of the molecule. The adiabatic, or strongly-coupled, limit corresponds to an infinite moment of inertia ($I \to \infty$) where the rotational band of the system collapses to the bandhead energy. In this section devoted to atomic systems, we will be using Rydberg units (energy expressed in Ry and distance in Bohr radius a_0).

One way to solve the coupled-channel equations (3.6) is by means of the direct integration method (DIM), but a reasonable initial guess is required to ensure convergence [4]; this can be difficult for those exotic systems whose components are not well known in advance. Also, higher-multipolarity potentials require a larger number of channels, which makes this method computationally demanding.

An alternative to the DIM is to use the basis expansion technique based on the Berggren ensemble. With the basis generated using the diagonal part of the potential V_{cc} [54] for each channel, this Berggren expansion method (BEM) provides a faster way of solving Eq. (3.6). Moreover, in this method, one can obtain all the eigenstates at once by diagonalizing the complex-symmetric Hamiltonian.

Finally, one needs to identify resonances from the non-resonant scattering background. This can be done by analyzing the internal wave function of an eigenstate or using the fact that resonances do not depend on a detailed choice of the contour [1]. Moreover, as a further test, the resonant states obtained in BEM are used in the DIM as an initial guess, and it is checked that the BEM results are reproduced.

3.2 Results for quadrupolar anions

In this section, we present the results for the quadrupolar anions with a focus on two aspects. One is the critical quadrupolar moments that binds the anion. The other is the coupling scheme between the molecule and valence electron in both above and below the dissociation threshold, with a focus on the transition between two regimes.

3.2.1 Critical quadrupolar moments

To test the precision of our model, we benchmark the DIM and BEM as applied to quadrupolar anions. Our results corrresponding to the adiabatic limit can be compared with the analytical results of Ref. [78] for the critical electric quadrupole moment $Q^{\pm}_{zz,c} = \pm 2 q^{\pm}_{s,c} s$. The internuclear distance s is fixed at $1.6\, a_0$ as in Ref. [3]; this value is close to the internuclear distance in CS_2^- ($s = 1.554\, a_0$ [79]). The corresponding critical quadrupole moments obtained analytically are $Q^{-}_{zz,c} = -2.35152\, e a_0^2$ and $Q^{+}_{zz,c} = 6.372016\, e a_0^2$.

In the DIM, the parameter that controls the accuracy of calculations is the orbital angular momentum cutoff $\ell_{\max}$ that determines the size of the channel basis. For $\ell_{\max} = 12$, the DIM gives a critical oblate quadrupole moment of $Q^{-}_{zz,c} = -2.35162\, e a_0^2$. In the BEM, in addition to $\ell_{\max}$, the momentum cutoff $k_{\max}$ needs to be fixed. By taking a real contour $\mathcal{L}^+$ discretized with 80 points, and $k_{\max} = 12\,a_0^{-1}$, one obtains $Q^-_{zz,c} = -2.35164\,ea_0^2$. The critical oblate quadrupole moment can be approached closely with both methods because it corresponds to a configuration of the attached electron that is well localized around the two positive charges at the center of the molecule. Thus, the electron is expected to be primarily in low-ℓ orbitals. For the prolate quadrupole moment, the situation is different. Here, the attached electron, attracted by the external positive charges, is less bound and higher-ℓ partial waves are expected to play a more important role. Indeed, as shown in Fig. 3.2, the DIM and BEM results do not reproduce the analytical value as precisely as for the oblate configuration. For $\ell_{\max} = 14$ and $k_{\max} = 12\,a_0^{-1}$, we obtained $Q^+_{zz,c} = 6.398\,ea_0^2$ and $Q^+_{zz,c} = 6.3984\,ea_0^2$ with the DIM and BEM, respectively. While the convergence of $Q^+_{zz,c}$ with $\ell_{\max}$ (and $k_{\max}$) is slower than for $Q^-_{zz,c}$, DIM and BEM results are fairly consistent for $\ell_{\max} = 14$ and $k_{\max} = 12\,a_0^{-1}$, and our results are in agreement with the DIM results of Ref. [3].

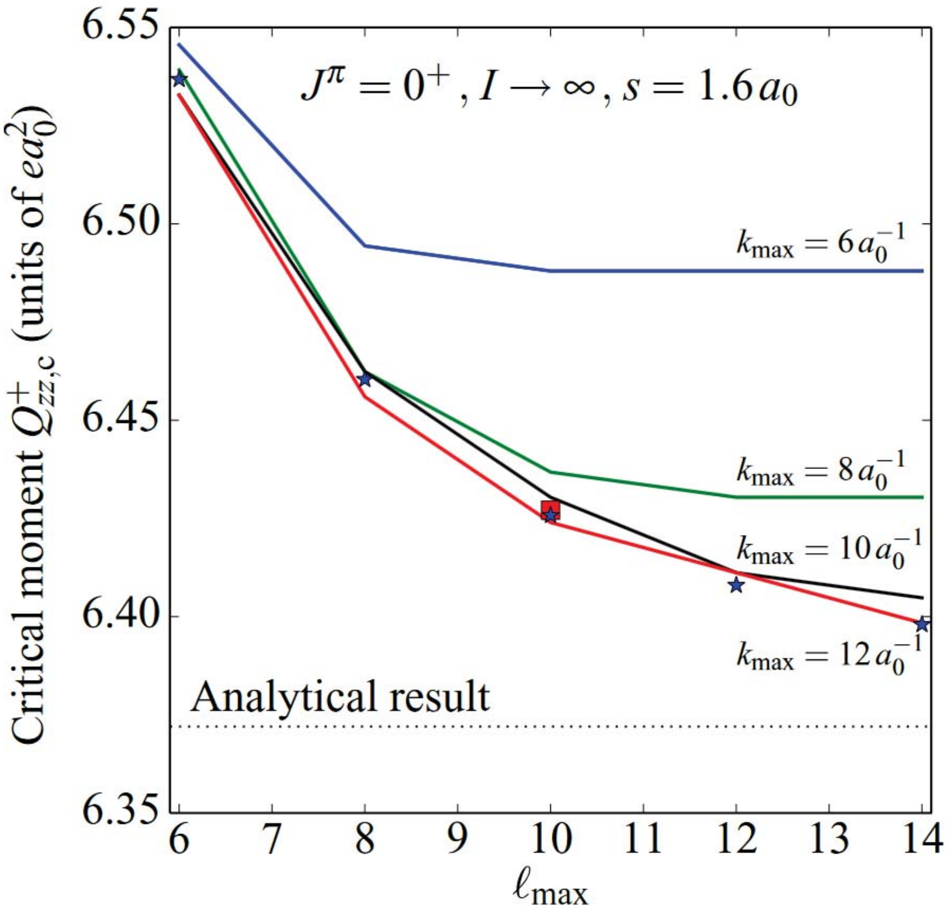

Figure 3.2: Critical prolate electric quadrupole moment as a function of the orbital angular momentum cutoff $\ell_{\max}$ in coupled-channel calculations in the adiabatic limit ($I \to \infty$) The internuclear distance is fixed at $s = 1.6\,a_0$ and the corresponding value of $Q^{+}_{zz,c} = 6.372016\,ea_0^2$ is indicated by the dotted line. The DIM results are marked by stars. The DIM result from [3] is denoted by a square at $\ell_{\max} = 10$. The convergence of the BEM results with respect to the momentum cutoff is shown for $k_{\max} = 6$,8,10,and $12\,a_0^{-1}$. Taken from Ref. [4].

In realistic molecules, the effect of Pauli blocking at short distances [80, 81, 82] reduces the binding in the oblate configuration; hence, in general, the prolate configuration is more likely to bind electrons. Thus, while our oblate configuration results are useful for benchmarking purposes, their physical interpretation should be dealt with caution.

3.2.2 Rotational bands in the continuum

In a previous study on dipolar anions [54], the yrast band has been predicted to disappear above the dissociation threshold, which implies a transition for anions going from below to above the threshold. Below the threshold, the motion of the attached election is strongly coupled to the rotational motion of the molecule. Above the threshold, however, the electron becomes weakly coupled and moves almost independently.

Compared with the dipolar potential ($\propto 1/r^2$), the quadrupolar potential has a faster asymptotic falloff ($\propto 1/r^3$) that may affect the structure of the delocalized resonant states. In order to see the structure of resulting rotational bands, the binding energy for $Q_{zz}^- = -2.42\, ea_0^2$ and $Q_{zz}^+ = +6.88\, ea_0^2$ is plotted in Fig. 3.3(a) and Fig. 3.3(b), respectively, as a function of $J(J+1)$.

Here we use the same parameters as in the previous section ($s = 1.6\, a_0$ and $I = 10^4\, m_e a_0^2$). The contour $\mathcal{L}_c^+$ is assumed to be identical for all partial waves: it starts at zero and is defined by the three points: $(0.3, -10^{-5}), (0.6, 0)$, and (6,0) (all in a_0^{-1}). The three resulting segments are discretized with 30, 30, and 40 scattering states, respectively. The specific values of Q_{zz} has been chosen so that the binding energy approaches zero for a total angular momentum $J \approx 2, 3$ at $\ell_{\max}$=4.

The BEM and DIM results are practically indistinguishable for all the values of $\ell_{\max}$ considered. Perfect rotational behavior is predicted for both prolate and oblate configurations, even above the dissociation threshold. This is confirmed by the collapse of all eigenenergies to the same bandhead energy in the adiabatic limit ($I \to \infty$). At the maximal orbital angular momentum cutoff $\ell_{\max}$ considered, the states in the lowest-energy (yrast) band are all dominated by the $\ell = 0$ channel at about 99.7% and 87.9%, for the oblate and prolate configuration, respectively. Unlike in the dipolar case, rotational bands of quadrupolar anions persist in the continuum.

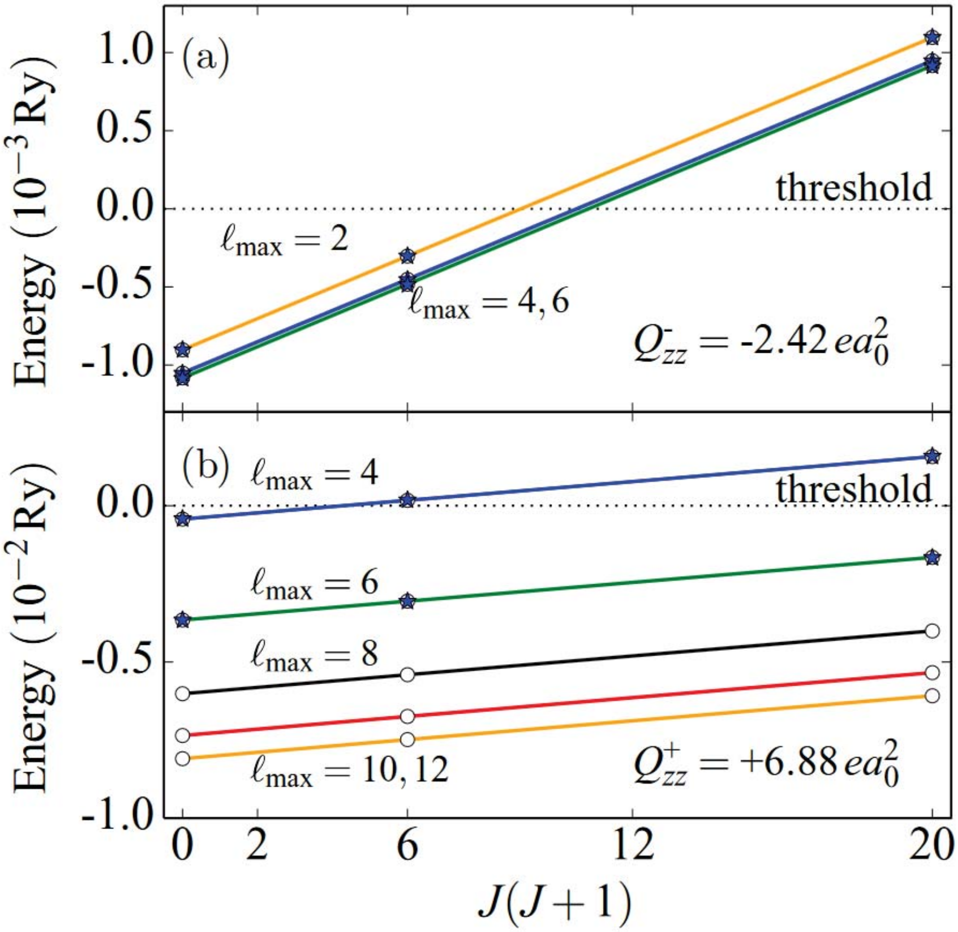

Figure 3.3: Yrast band of quadrupolar anions defined by an internuclear distance of $s = 1.6\,a_0$, a moment of inertia of $I = 10^4\,m_e a_0^2$, and quadrupole moments of $Q^{-}_{zz}{=}{-}2.42\,ea_0^2$ and $Q^{+}_{zz}{=}{+}6.88\,ea_0^2$ on panels (a) and (b), respectively. The BEM and DIM results are denoted with empty circles and stars, respectively, and are almost indistinguishable for all orbital angular momentum cutoffs considered. Taken from Ref. [4].

3.3 Results for anions bounded by multipolar Gaussian potentials

In the section, we investigate the generic near-threshold behavior of multipole-bound anions at the transition between the subcritical (below dissociation threshold) and supercritical (above dissociation threshold) regimes. The main objective of this part is to show the role of low-ℓ partial waves in shaping the properties of low-lying states. We assume that the molecular potential has a Gaussian form given by Eq. (3.4). However, we wish to emphasize that the particular choice of the radial form factor is not important as it represents an a priori unknown short-range behavior. One can view this particular realization as a regularized zero-range interaction. To study the threshold behavior of the system we investigate the pattern of resonant poles as a function of four parameters: the strength and range of the Gaussian form factor, the multipolarity of the potential, and the molecular moment of inertia.

3.3.1 Threshold trajectories for multipolar Gaussian potentials in the adiabatic limit

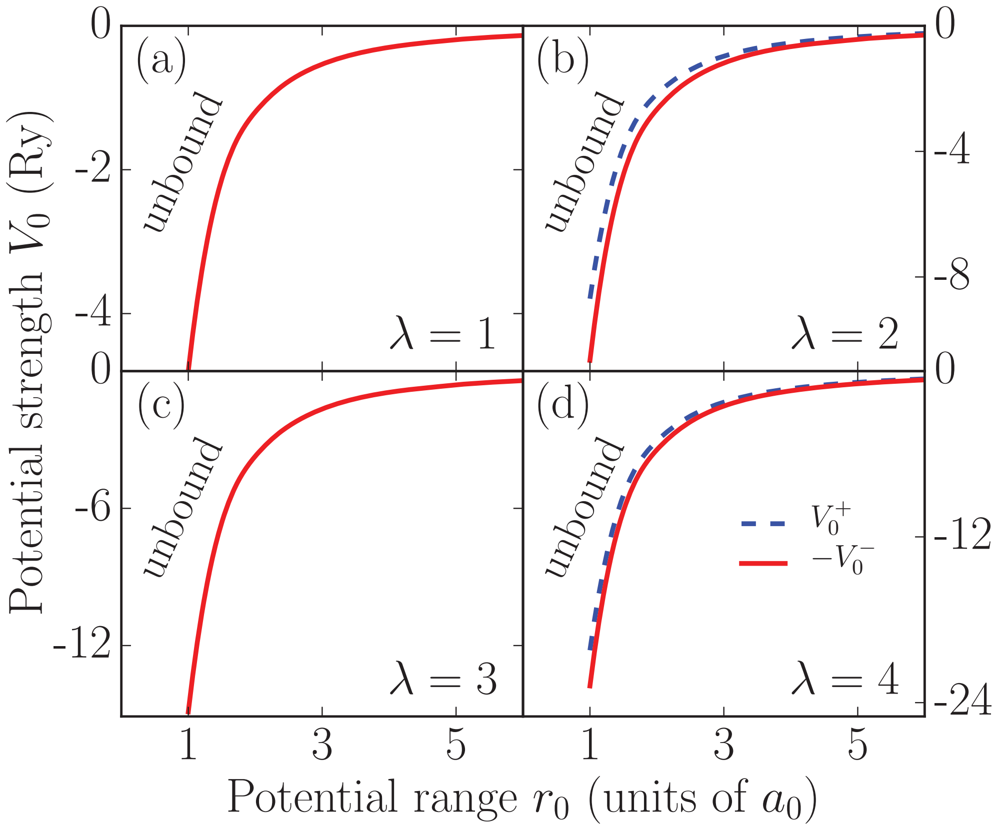

Figure 3.4: Threshold trajectories $(V_0, r_0)_c^{\pm}$ for multipolar Gaussian potentials with $\lambda = 1 - 4$ in the adiabatic limit. Taken from Ref. [2].

As mentioned earlier, the critical multipole moments $Q^{\pm}_{\lambda,c}$ mark the limit between the subcritical and supercritical regimes. One may notice that $Q^{-}_{\lambda,c} = -Q^{+}_{\lambda,c}$ for odd-multipolarity potentials, but there is no such relation for even multipolarity potentials. As discussed earlier, there are two critical values of the quadrupole moment for a quadrupole-bound anion ($\lambda = 2$): $Q^{+}_{2,c}$ (prolate) and $Q^{-}_{2,c}$ (oblate), and $Q^{-}_{2,c} \neq -Q^{+}_{2,c}$.

As the usual $-1/r^{\lambda+1}$ radial dependence of multipolar potentials is replaced in our work by the Gaussian form factor, the dissociation threshold is obtained at the critical trajectories of $(V_0, r_0)_c^{\pm}$. Fig. 3.4 shows such trajectories obtained in the adiabatic limit for the $J^\pi = 0_1^+$ g.s. of anions with multipolarities $\lambda = 1 - 4$.

These results are obtained with a Berggren contour defined by the points $k_{\text{peak}} = (0.5, -0.1)$, $k_{\text{mid}} = 1.0$, and $k_{\text{max}} = 14.0$ (in units of a_0^{-1}), with each segment being discretized by 40 Gauss-Legendre points. To ensure convergence, we took $\ell_{\text{max}} = 4$ for $\lambda = 1, 2, 3$ and $\ell_{\text{max}} = 8$ for $\lambda = 4, 5$.

As one would expect, the absolute value of the critical potential strength $|V_{0,c}|$ required to bind an excess electron decreases with the range r_0 and for a fixed range $|V_{0,c}|$ increases with multipolarity. Also, as noted in previous studies [83, 78, 84, 4], for even multipolarities, the value of $|V_{0,c}|$ for negative-V_0 potentials ("prolate") is larger than that for positive-V_0 potentials ("oblate").

It is interesting to note that at the threshold the wave functions are dominated by the $\ell = 0$ component. Dividing the intrinsic wave function into the inner region ($r < R$) and outer region ($r > R$) contributions, where R is the distance at which the molecule potential becomes practically unimportant, one can show [85, 86, 87] that the probability of finding the electron in the outer region approaches one at the dissociation threshold if the $\ell = 0$ component is present in the intrinsic wave function. This has been practically demonstrated in our work on quadrupole-bound anions [4] in the context of the scaling properties of root-mean-square (rms) radii.

3.3.2 Resonances of the near-critical quadrupolar Gaussian potential

In order to study the role of low-ℓ partial waves on the structure of multipole-bound anions, one has to recognize the impact of $\ell = 0$ partial waves on resonant states near threshold [87]. In our coupled-channel formalism, resonant states appear through the mixing of different channels. To study general features of near-threshold resonances, we consider three states of the quadrupolar potential in the adiabatic approximation. Namely, we investigate: (i) the $J^\pi = 0_1^+$ g.s. dominated by the $\ell = 0$ partial wave; (ii) an excited $J^\pi = 0_d^+$ state dominated by the $\ell = 2$ channel; and (iii) the lowest $J^\pi = 1_1^-$ state, which is primarily $\ell = 1$ and without contribution from $\ell = 0$. The quadrupolar case discussed here is characteristic of other multipolar potentials.

(i) Resonant states dominated by the $\ell = 0$ channel

The g.s. of the quadrupolar potential is computed with the BEM, using the extended contour $\mathcal{L}^+$ defined by the points: $k = (0, 0)$, $(-0.1, -0.4)$, $(0.1, -0.4)$, $(2, 0)$, and $(14, 0)$ (all in a_0^{-1}), each segment being discretized with 40 Gauss-Legendre points. By considering the contour that extends into the third quadrant of the complex-momentum plane, antibound states can be revealed [1, 88, 89].

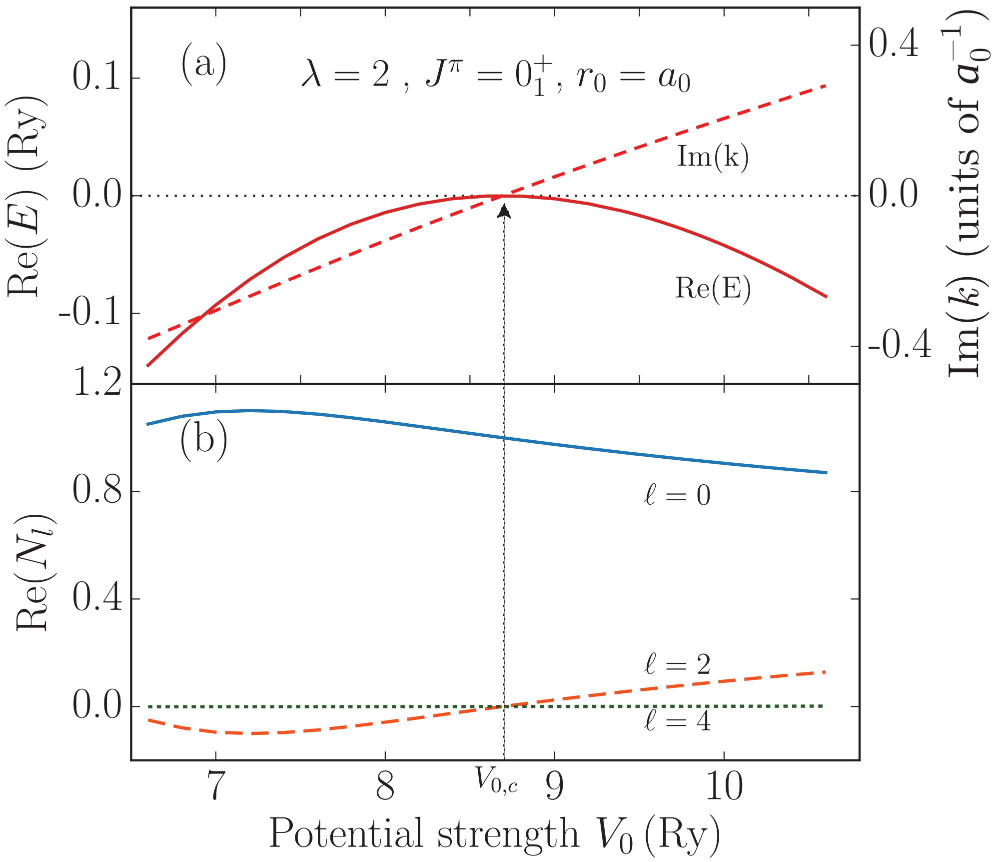

Figure 3.5: The lowest 0^+ resonant state of the quadrupolar Gaussian potential with $r_0 = a_0$ as a function of V_0. Top: real energy and imaginary momentum. Bottom: the channel decomposition of the real part of the norm. The critical strength $V_{0,c}$ is marked by arrow. Taken from Ref. [2].

Fig. 3.5(a) shows the energy and momentum of the 0^+_1 state for different values of the potential strength V_0. For large values of V_0, the g.s. is bound (Re(E)<0) and has a positive imaginary momentum. As the potential strength decreases, the energy of the g.s. moves up and approaches the $E = 0$ threshold at $V_{0,c} = 8.7\,\mathrm{Ry}$. For $V_0 < V_{0,c}$ the lowest 0^+ state becomes antibound (Re(E) < 0, Im(k) < 0). As illustrated in Fig. 3.5(b), the contributions N_ℓ to the complex norm of the wave function from different ℓ-channels ($\ell = 0, 2,\ 4$) vary smoothly when crossing the threshold. The norm is largely dominated by the $\ell = 0$ component. At the critical strength, the $\ell > 0$ contributions to the norm vanish, cf. discussion in Sec. 3.3.1. This indicates that the presence of near-threshold antibound states indeed impacts the structure of the low-energy continuum [90, 91, 92, 93, 34].

(ii) Resonant states dominated by a $\ell \neq 0$ channel

We now consider the evolution of an excited state of a wider quadrupolar potential with $r_0 = 4\,a_0$. At V_0 =1.1 Ry, the lowest 0^+ state is bound and the second $J^\pi = 0^+_2$ state is a decaying resonance, see Fig. 3.6. Figure 3.7(a) shows the channel decomposition for this second 0^+_2 state. It is seen that its configuration has the predominant $\ell = 2$ component.

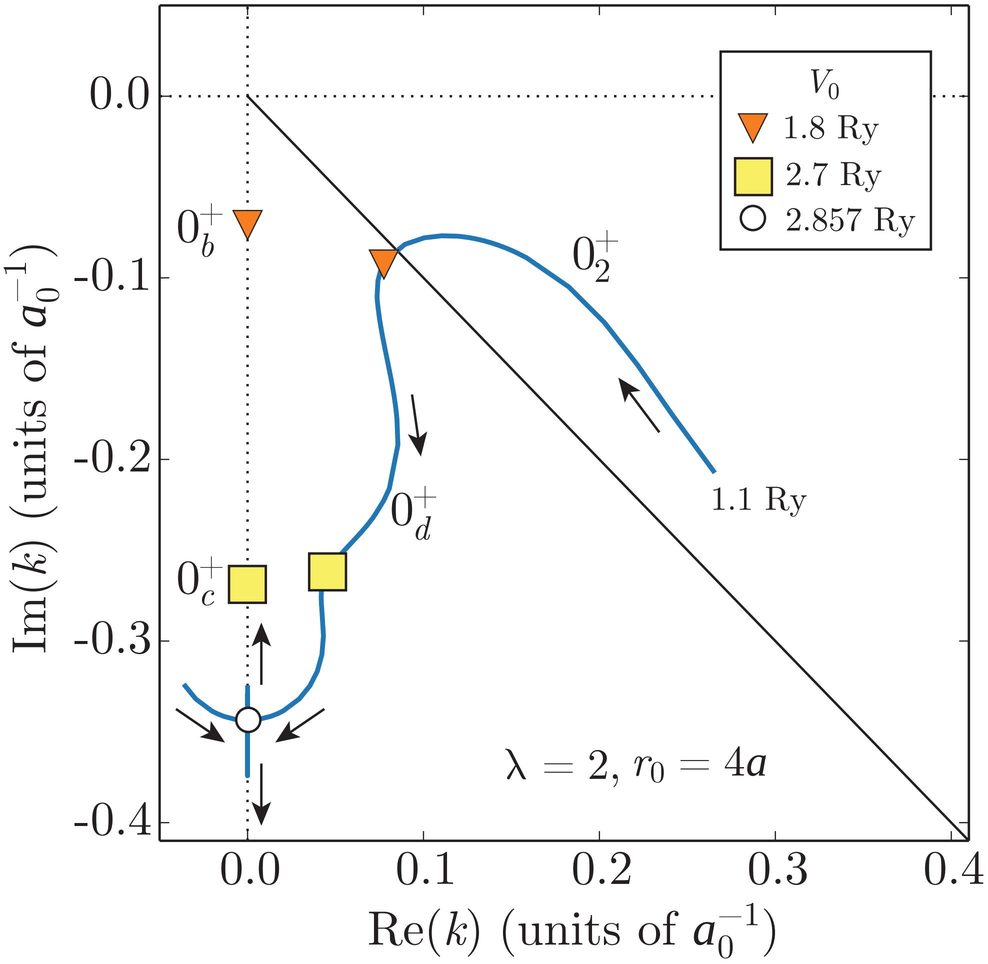

Figure 3.6: Trajectory of the 0^+ resonant state in the complex-k plane of the quadrupolar potential with $r_0 = 4\,a_0$ as the potential strength V_0 increases in the direction indicated by an arrow. At the lowest value V_0 =1.1 Ry, the 0^+ g.s. is bound and the state of interest is an excited 0_2^+ state associated with a decaying resonance. At $V_0 = 1.8$ Ry the pole crosses the $-45°$ line and becomes a subthreshold resonance 0_d^+. At $V_0 = 2.857$ Ry the decaying pole reaches the imaginary-k axis and coalesces with the capturing pole with $\mathrm{Im}(k) < 0$ forming an exceptional point. The antibound states at $V_0 = 1.8$ Ry and $V_0 = 2.7$ Ry are marked. Taken from Ref. [2].

As the potential gets deeper, the pole crosses the $-45°$ line at $V_0 \approx 1.8$ Ry and becomes a subthreshold resonance labeled as 0_d^+. At $V_0 = 2.7$ Ry, a rapid transition to a configuration dominated by the $\ell = 4$ partial wave takes place, which is indicative of a level crossing in the complex-k plane. At $V_0 = 2.857\,\mathrm{Ry}$ the decaying pole arrives at the imaginary-k axis and coalesces with the symmetric capturing pole forming an exceptional point [94, 95, 96]. At still larger values of V_0, the exceptional point splits up into two antibound states moving up and down along the imaginary-k axis as shown in Fig. 3.6. A similar situation was discussed in Refs. [42, 97] in the context of electron-molecule scattering and optical lattice arrays, respectively.

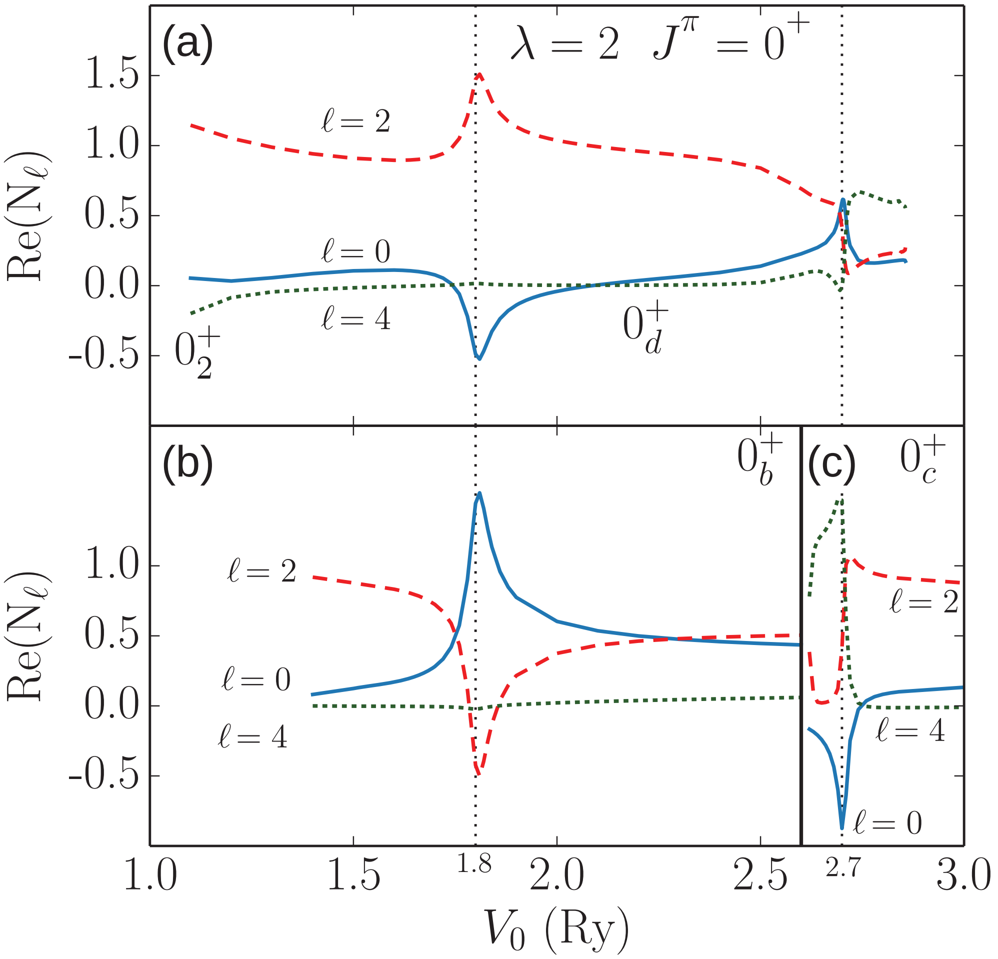

Figure 3.7: Real norms of the channel wave functions for the decaying pole 0_d^+ shown in Fig. 3.6 and the antibound states 0_b^+ and 0_c^+ of Fig. 3.8. Taken from Ref. [2].

In the range of V_0 corresponding to the trajectory $0_2^+ \to 0_d^+$ shown in Fig. 3.6, there appear antibound states in the threshold region. Their trajectories along the imaginary-k axis are shown in Fig. 3.8 and their channel decompositions are given in Fig. 3.7(b) and (c). As V_0 increases, the antibound states 0_a^+, 0_b^+, and 0_c^+ emerge as bound physical states of the system labeled as 0_1^+, 0_2^+, and 0_3^+, respectively. The lowest antibound state 0_a^+ has a dominant $\ell = 0$ configuration, similar to that of Fig. 3.5. At low values of V_0, the wave function of the antibound state 0_b^+ is predominantly $\ell = 2$. As seen in Fig. 3.6, this state appears close to the decaying pole 0_d^+ at $V_0 \approx 1.8\,\mathrm{Ry}$ and the crossing between these two poles in the complex-k plane is seen in their wave function decompositions. Following the crossing, the state 0_b^+ acquires a large $\ell = 0$ component. The antibound state 0_c^+ begins as an $\ell = 4$ configuration. At $V_0 \approx 2.7\,\mathrm{Ry}$, this state interacts with 0_d^+ and its configuration changes to $\ell = 2$. One can thus see that the presence of antibound states results in the particular shape of the 0_d^+-pole trajectory in the complex-k plane.

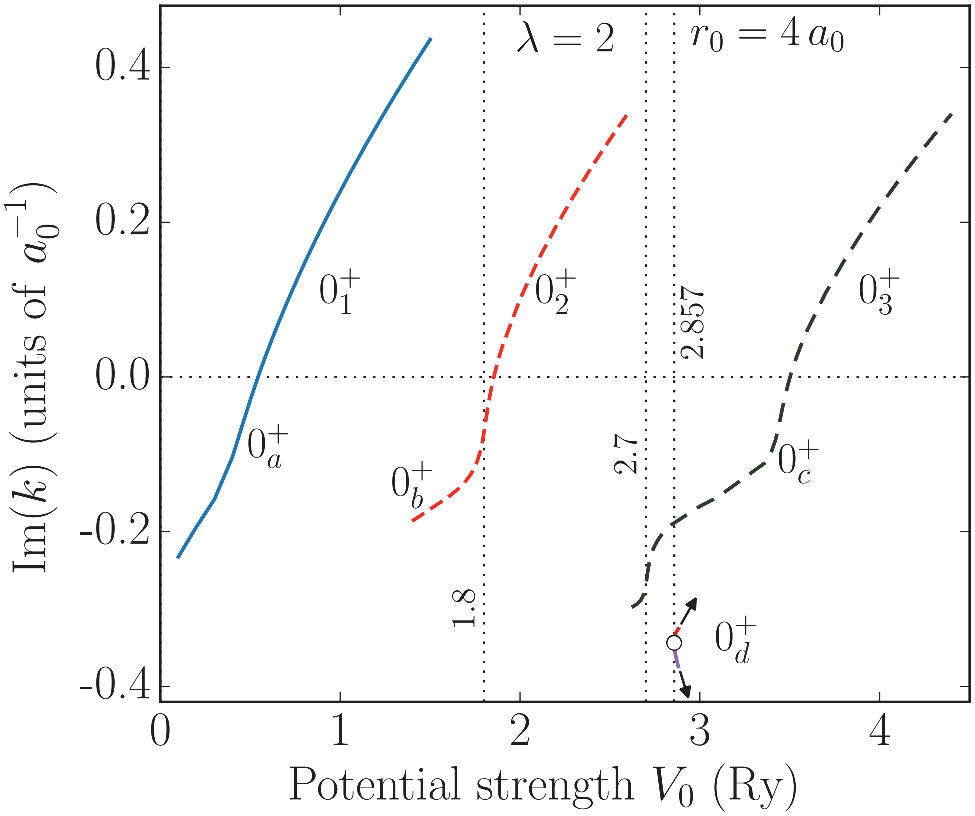

Figure 3.8: Trajectories of antibound and bound 0^+ states along the imaginary-k axis as a function of V_0 for the quadrupolar potential with $r_0 = 4\,a_0$. With increasing potential strength, the antibound states 0^+_a, 0^+_b, and 0^+_c become bound states of the system 0^+_1, 0^+_2, and 0^+_3, respectively. The open circle marks the exceptional point of Fig. 3.6, which is the source of two antibound states. The particular values of V_0 discussed around Fig. 3.6 are marked. Taken from Ref. [2].

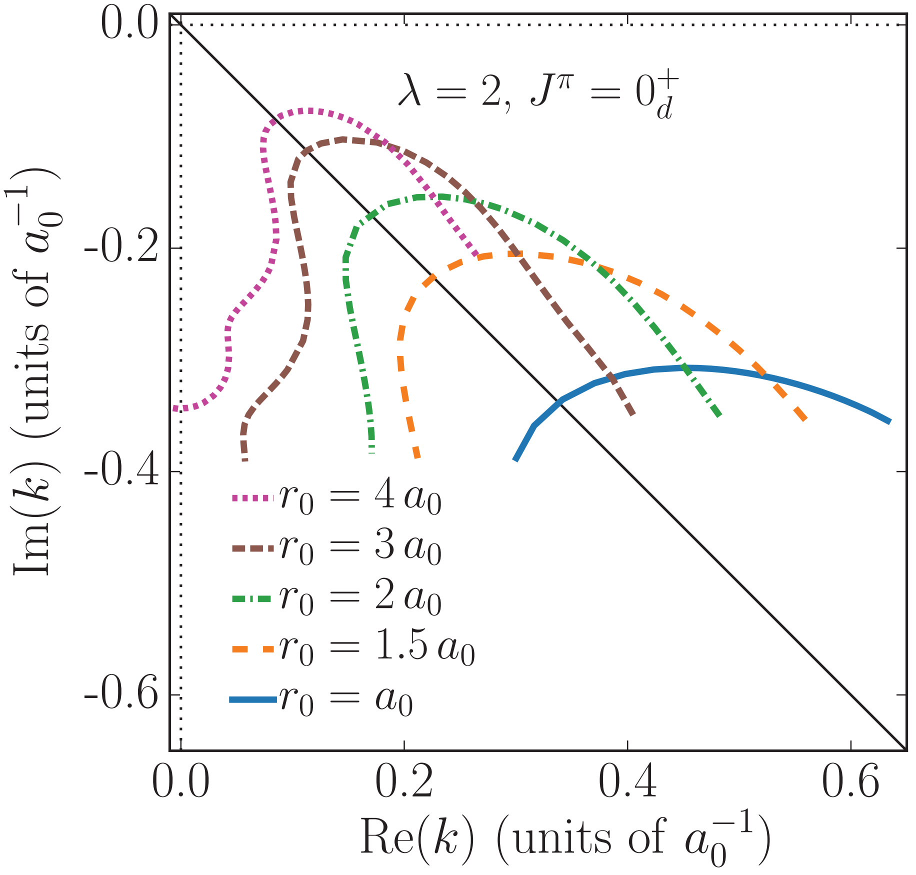

Figure 3.9: Trajectory of the 0_d^+ resonant state in the complex-k plane for different values r_0 of quadrupolar potential as indicated by numbers (in units of a_0). The ranges of V_0 (in Ry) are: (25.6-29.0) for $r_0 = a_0$; (9.7-14.5) for $r_0 = 1.5\,a_0$; (4.8-10) for $r_0 = 2\,a_0$; (1.7-4.79) for $r_0 = 3\,a_0$; and (1.1-2.85) for $r_0 = 4\,a_0$. Taken from Ref. [2].

The dependence of the 0_d^+-pole trajectory on the potential range is illustrated in Fig. 3.9. For potentials with longer ranges, pole trajectories appear closer to the origin. Due to the numerical stability issue, the contour used can not go below $-0.4\,a_0^{-1}$ for imaginary momentum. Consequently, a wider potential with $r_0 = 4\,a_0$ is chosen so that the whole complex-momentum trajectory can be revealed. In all the cases shown, a transition from decaying to subthreshold resonances takes place. These poles have large widths and are expected to impact the structure of the low-energy scattering continuum.

(iii) Resonant states without a $\ell = 0$ component

Here we discuss the lowest $J^\pi = 1_1^-$ state, which is primarily $\ell = 1$ with a small admixture of the $\ell = 3$ channel. This case closely follows the discussion of Ref. [42] for p-wave scattering from short-range potentials.

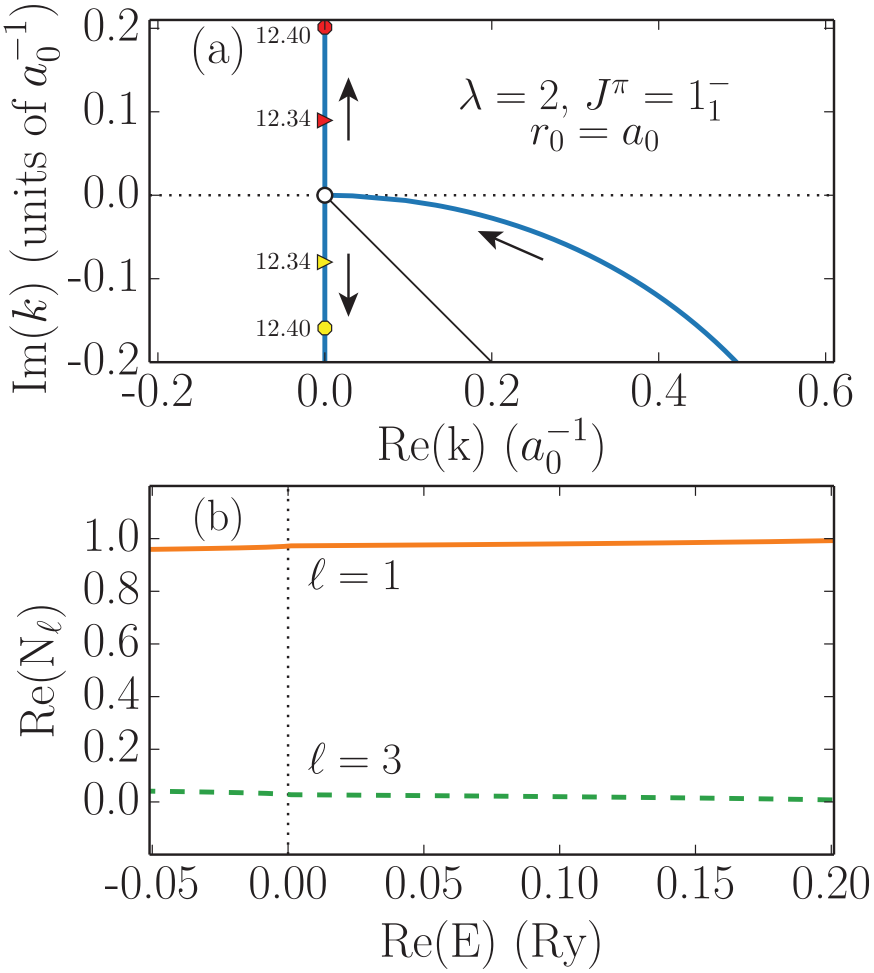

Figure 3.10: Top: trajectory of the lowest 1_1^- resonant state of the quadrupolar potential with $r_0 = a_0$ as a function of V_0 in the range of (9-12.7) Ry. The potential strength V_0 increases along the direction indicated by an arrow. The positions of the bound and antibound states at $V_0 = 12.34$ Ry and 12.4 Ry are marked. Bottom: real norms of channel functions for this state. Taken from Ref. [2].

The corresponding trajectory of this state in the complex-momentum plane is shown in Fig. 3.10(a). At larger values of V_0, the 1_1^- state is bound. As V_0 decreases, this state crosses the dissociation threshold and becomes a narrow decaying resonance. The trajectory of the capturing resonance, symmetric with respect to the imaginary-(k) axis, is not shown.

As discussed in Ref. [42], the exceptional point appears at the origin at $V_{0,c}$. Close to the threshold, the bound state and the antibound state are located symmetrically to the origin. For the p-wave dominated state, the transition from the subcritical to the supercritical regime is smooth, i.e., the wave function amplitudes hardly change with V_0, see Fig. 3.10(b). This is because the contributions from antibound and bound poles cancel each other out. In this case, the structure of the low-energy continuum is not expected to be affected by the presence of threshold poles.

The situation presented in Fig. 3.10 is rather generic for p-wave dominated resonant poles. Increasing the potential range moves the pole trajectory closer to the real-k axis. Consequently, states containing no s-wave component are likely to appear as isolated narrow resonances. For odd-multipolarity potentials, a $(j = J, \ell = 0)$ component of a J^π state becomes large as the dissociation threshold is approached, see Sec. 3.3.2. On the other hand, for even-multipolarity potentials, odd-J states cannot have an s-wave component, as the molecule's angular momentum j must be even, and narrow near-threshold resonances can appear.

3.3.3 Rotational motion

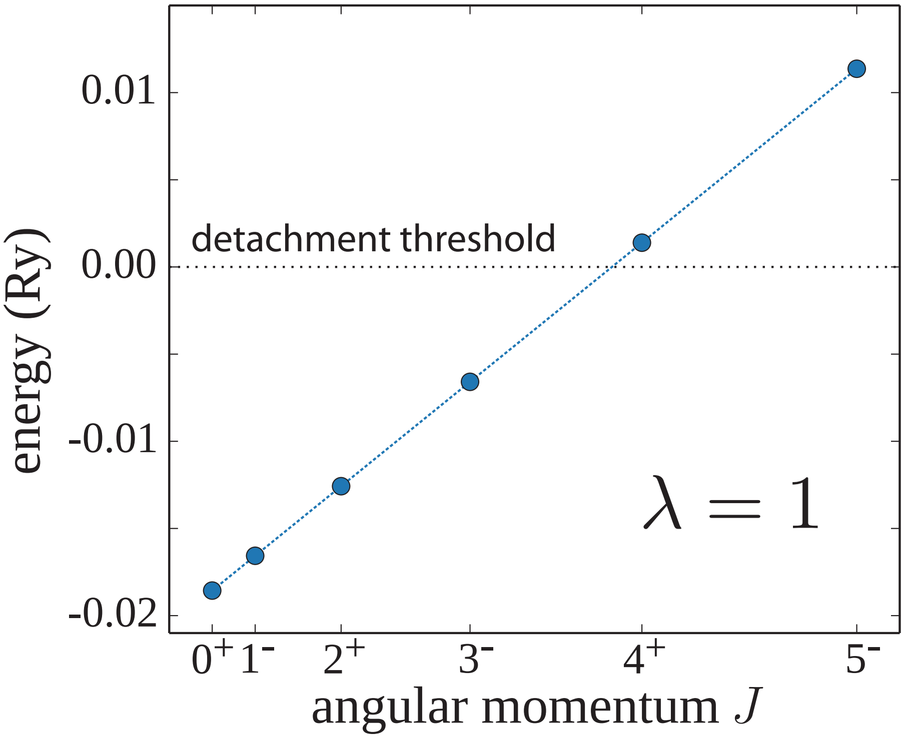

Figure 3.11: The rotational band built upon the $J^\pi = 0_1^+$ state of a dipole-bound anion. The parameters $V_0 = 5.33\,\mathrm{Ry}$, $r_0 = a_0$, and $I = 10^3\, m_e a_0^2$ have been chosen to place the bandhead energy slightly below the zero-energy threshold, where the rotational motion of the molecule can excite the system into the continuum. The energy is plotted as a function of $J(J+1)$. Taken from Ref. [2].

To describe multipole-bound anions, one has to take into account the nonadiabatic coupling between the rotational motion of the molecule and the s.p. motion of the electron. Whether a multipole-bound anion can exhibit rotational bands depends on multipolarity. For instance, it was shown in Ref. [54] that rotational bands of dipolar anions do not extend above the dissociation threshold while a similar study for quadrupole-bound anions [4] demonstrated that the rotational motion of the anion is hardly affected by the continuum.

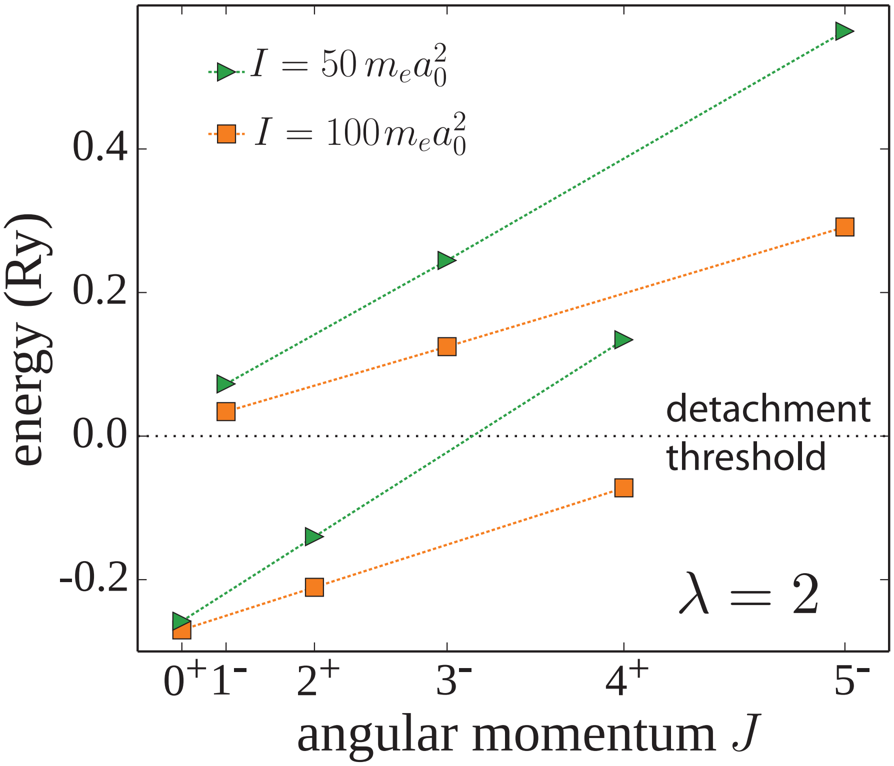

Figure 3.12: Similar to Fig. 3.11 but for rotational bands built upon the $J^\pi = 0_1^+$ and 1_1^- bandheads of a quadrupolar Gaussian potential with $V_0 = 12.38\,\mathrm{Ry}$, $r_0 = a_0$, and for $I = 50\, m_e a_0^2$ and $I = 100\, m_e a_0^2$. Taken from Ref. [2].

Figure 3.11 illustrates the case of a rotational band built upon the subthreshold $J^\pi = 0_1^+$ state of the dipolar Gaussian potential. It is seen that the rotational band is not affected when the zero-energy threshold is crossed below $J = 4$. This result indicates that the presence of the two coupling regimes predicted to exist in realistic calculations for dipole-bound anions [54] must be due to difficulties in imposing proper boundary conditions at infinity for the dipolar potential ($\sim r^{-2}$) when the rotational motion of the molecule is considered nonadiabatically [77]. Since in the present work the radial part of the dipolar pseudopotential is replaced by a Gaussian function, the outgoing boundary condition can be readily imposed.

We now investigate the impact of the molecular rotation on the energy spectrum of the anion. By definition, changing the moment of inertia of the molecule is expected to have a larger effect on states dominated by channels with large j, but in practice, such channels are unlikely to dominate at low energies. As an illustrative example, we study the 3_1^- state of the quadrupolar ($\lambda = 2$) Gaussian potential. Figure 3.13(a,b) shows, respectively, the energy and decay width of the 3_1^- resonance as a function of the potential strength and the inverse moment of inertia.

A similar result is obtained for the quadrupolar case shown in Fig. 3.12 for two rotational bands built upon the $J^\pi = 0_1^+$ and 1_1^- bandheads. The existence of rotational bands extending above the dissociation threshold is consistent with the findings of Ref. [4] employing the realistic quadrupolar pseudopotential. The results for higher-multipolarity potentials follow the pattern obtained for the dipolar and quadrupolar cases; hence, they are not shown here.

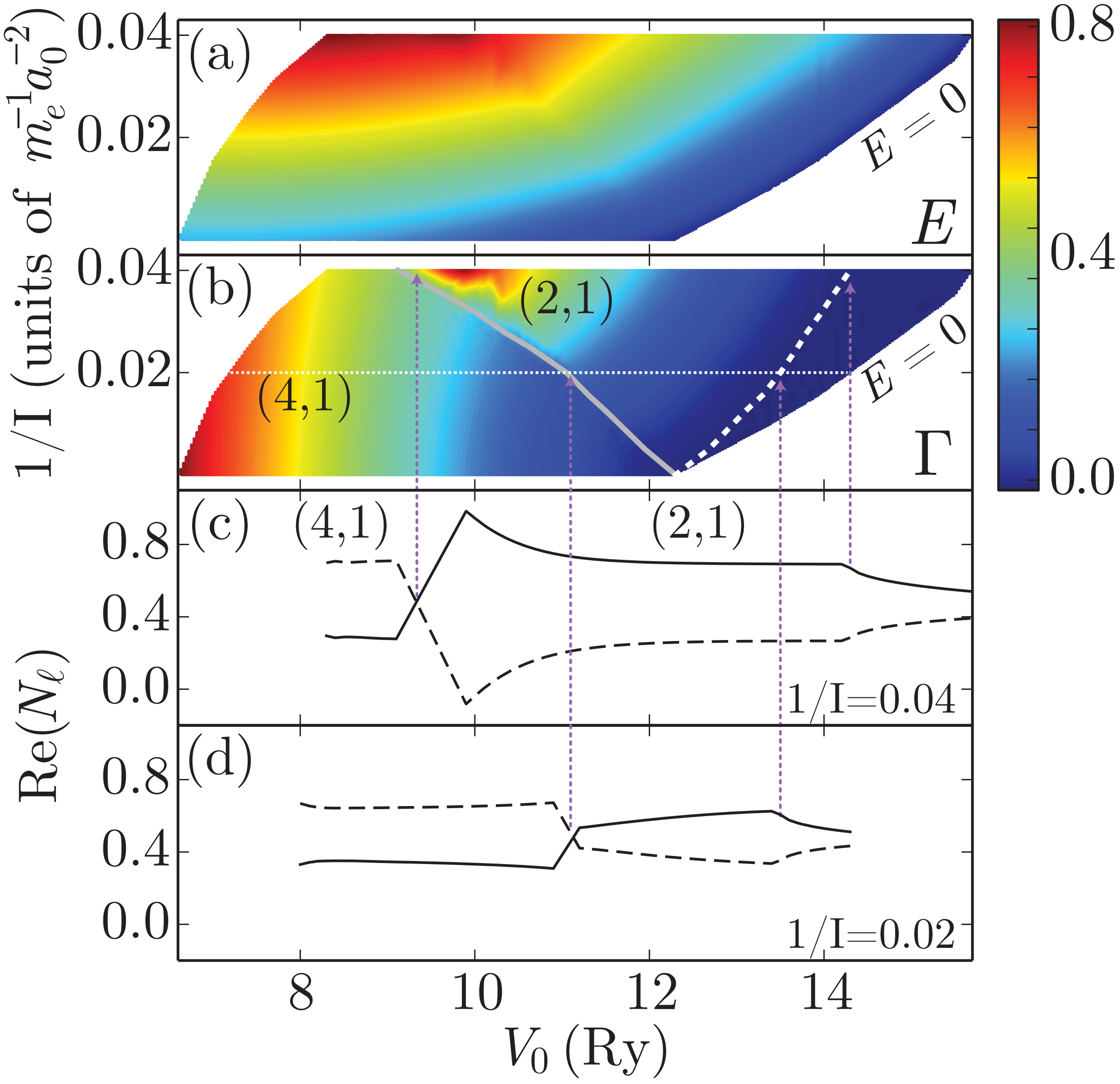

Figure 3.13: Energy (a) and decay width (b), both in Ry, of the 3_1^- resonance of the quadrupolar Gaussian potential with $r_0 = a_0$ as a function of the inverse of the moment of inertia and the potential strength. The dissociation threshold ($E = 0$) is indicated. The dominant (j, ℓ) channel is marked in panel (b). When the rotational energy of the molecule $E_{\rm rot}^{j=4}$ lies below/above the energy of the 3_1^- resonance, the (4,1) decay channel is open/closed. The line $E_{\rm rot}^{j=4} = E(3_1^-)$ (thick solid) separating these two regimes is marked, so is the line $E_{\rm rot}^{j=2} = E(3_1^-)$ (thick dotted) which corresponds to the threshold energy for the opening of the (2,1) channel. The norms of the two dominant channels (2,1) (solid line) and (4,1) (dotted line) are shown as a function of V_0 for $1/I = 0.04\, m_e^{-1} a_0^{-2}$ (c) and $0.02\, m_e^{-1} a_0^{-2}$ (d). Taken from Ref. [2].

At large values of V_0 when the 3_1^- resonance lies close to the threshold, its wave function is primarily described in terms of two channels with $(j, \ell) = (2, 1)$ and $(4, 1)$ with the dominant (2,1) amplitude, see Fig. 3.13(c,d). At a finite value of I, as the energy of the resonance increases, a transition takes place to a state dominated by the (4,1) component that is associated with a reduction of the decay width. This transition can be explained in terms of channel coupling. At very low values of $1/I$, the energy $E(3_1^-)$ lies above the rotational 4^+ state of the molecule. As the moment of inertia decreases, the 4^+ member of the g.s. rotational band of the molecule moves up in energy, and at some value of I it becomes degenerate with the energy of the $E(3_1^-)$ resonance, i.e., $E_{\rm rot}^{j=4} = E(3_1^-)$. At still higher values of $1/I$, the (4,1) channel is closed to the electron emission. As seen in Fig. 3.13(b), the irregular behavior in the width of the resonance can be attributed to the (4,1) channel closing effect [98]. A second irregularity in Fig. 3.13(c,d), seen at large potential strengths, corresponds to $E_{\rm rot}^{j=2} = E(3_1^-)$. As the resonance approaches the threshold, its tiny decay width can be associated with the (0,3) channel. Due to its higher centrifugal barrier, (0,3) channel contributes around 1% to the total norm in the threshold region.

Chapter 4

Lithium isotopes and mirror nuclei

4.1 Introduction

In the light-nuclei region of the nuclear landscape, the imbalance between proton and neutron numbers can reach high values, which is susceptible to continuum effects due to the presence of low-lying decay channels. Wave functions of such systems often "align" with the nearby threshold and are expected to have substantial overlaps with the corresponding decay channels. Among them, lithium isotopes are of particular interest as they reveal rich phenomena, including the binary cluster (α+d) of ^{6}Li [99, 100], the anitbound (virtual) state of ^{10}Li [43, 44, 45, 46], as well as the spatially extended halo structure of ^{11}Li [17, 24, 101].

However, such OQSs pose many challenges for nuclear thoery, since drip line nuclei can not be described in a typical HO-based configuration interaction method. As a result, for instance, the theoretical descriptions of ^{11}Li are usually based on a few-body approximation, including Faddeev equation [102] and other similar techniques [103, 104, 105, 106]. In this case, ^{11}Li is described as a loosely bound three-body system (^{9}Li core and two valence neutrons), due to its Borromean property [17, 24, 101], in which none of the two-body subsystems is bound.

One of the main drawbacks of a cluster approximation is that the core polarization effects are expected to be large, therefore, a more elaborated approach is required. To this end, we adopt GSM based on the BEM technique introduced in Chapters 2 and 3, which can give a comprehensive description of the interplay between many-body correlation and continuum coupling.

In this work, we study the lithium isotopes ($^{6-11}$Li) with a realistic residual interaction including uncertainty estimation of the Hamiltonian parameters as well as predicted spectra.

Another interesting aspect existing only in nuclear OQSs is the asymmetry between proton and neutron thresholds. This can result in different asymptotic behavior of proton and neutron wave functions resulting in the Thomas-Ehrman effect (TEE) [107, 108]. To study the TEE, the mirror partner of lithium isotopes have also been studied in this work.

4.2 Gamow shell model

4.2.1 Hamiltonian

The lithium isotopes and their mirror partners are studied in terms of valence nucleons coupled to the ^{4}He core. This is justified by the strongly bound nature of ^{4}He, whose first excited state is 20.21 MeV above the g.s. [7]. In this picture, the Hamiltonian is given as a sum of an s.p. core-nucleon potential and effective two-body interactions among the valence nucleons. In the intrinsic frame of the Cluster Orbital Shell Model (COSM) [109], where the nucleon coordinates are defined with respect to the center of mass of the core, the GSM Hamiltonian is expressed as:

$$H = \sum_{i}^{n} \left[\frac{p_i^2}{2\mu_i} + U_{\text{core}}(i) \right] + \sum_{i=1, i<j}^{n} \left[V_{i,j} + \frac{p_i p_j}{M_{\text{core}}} \right] \tag{4.1}$$

where n denotes number of valence nucleons, μ_i and M_{core} are the reduced mass of valence nucleon and core, respectively, and U_{core}, $V_{i,j}$ are the core-nucleon potential and nucleon-nucleon interaction, respectively. The last term in Eq. (4.1) is the recoil term in the COSM coordinates, which is used to eliminate the energy contribution from the center-of-mass motion. In GSM, to account for the many-body correlations, Slater determinants are built upon the discretized s.p. Berggren basis states of each shell to serve as the many-body basis within which the complex-symmetric H is diagonalized [1].

Core potential

The core-nucleon potential is taken as a Woods-Saxon (WS) field, with a central and spin-orbit term and Coulomb field for protons.

$$U_{\text{core}}(r) = V_0 f(r) - 4V_{\ell s} \frac{1}{r} \frac{df(r)}{dr} \boldsymbol{\ell} \cdot \boldsymbol{s} + U_{\text{Coul}}(r), \tag{4.2}$$

where $f(r) = -(1 + \exp[(r - R_0)/a])^{-1}$. The WS radius and diffuseness parameters were taken from Ref. [110]: $R_0(n) = 2.15$ fm, $R_0(p) = 2.06$ fm, $a(n) = 0.63$ fm, and $a(p) = 0.64$ fm. The Coulomb potential is generated by a spherical Gaussian charge distribution with the radius $R_{ch} = 1.681$ fm [111]. The strength of the central and the spin-orbit part of the potential, represented as V_0 and $V_{\ell s}$, respectively, are optimized in the work with respect to the selected states.

Two-body interaction

The effective two-body interaction is constructed based on the finite-range Furutani-Horiuchi-Tamagaki (FHT) force [110, 112, 113], which has been shown to successfully describe structure and reactions involving light nuclei [114, 110, 115, 116, 117].

The FHT interaction contains central (c), spin-orbit (LS), tensor (T) and Coulomb terms:

$$V = V_c + V_{LS} + V_T + V_{\mathrm{Coul}}. \tag{4.3}$$

The central and tensor parts are both a sum of three Gaussian functions with different ranges representing the short, intermediate and long ranges of nucleon-nucleon interaction. The spin-orbit part is a sum of two Gaussian functions [110]. In order to be applied in the present GSM formalism, the interaction is rewritten in terms of the spin-isospin projectors Π_{ST}:

$$\begin{aligned} V_c(r) =& V_c^{11} f_c^{11}(r)\Pi_{11} + V_c^{10} f_c^{10}(r)\Pi_{10} \\ &+ V_c^{00} f_c^{00}(r)\Pi_{00} + V_c^{01} f_c^{01}(r)\Pi_{01}, \end{aligned} \tag{4.4}$$

$$V_{LS} = (\boldsymbol{L}\cdot\boldsymbol{S}) V_{LS}^{11} f_{LS}^{11}(r)\Pi_{11}, \tag{4.5}$$

$$V_T(r) = S_{ij}[V_T^{11} f_T^{11}(r)\Pi_{11} + V_T^{10} f_T^{10}(r)\Pi_{10}], \tag{4.6}$$

where $r \equiv r_{ij}$ stands for the distance between the nucleon i and j, $\hat{r} = \boldsymbol{r}_{ij}/r_{ij}$, $\boldsymbol{L}$ is the relative orbital angular momentum, $\boldsymbol{S} = (\boldsymbol{\sigma}_i + \boldsymbol{\sigma}_j)/2$, and $S_{ij} = 3(\boldsymbol{\sigma}_i\cdot\hat{r})(\boldsymbol{\sigma}_j\cdot\hat{r}) - \boldsymbol{\sigma}_i\cdot\boldsymbol{\sigma}_j$. There are seven interaction strengths

V_η^{ST} ($\eta = c, LS, T$) in different spin-isospin channels, which are adjusted to experimental data.

In Ref. [110], the FHT interaction was used in the GSM description of bound and unbound nuclei with $A \leq 9$. While a good energy reproduction was achieved, the systematic statistical study of the parameters carried out in Ref. [110] demonstrated that some of the terms in the FHT interaction were sloppy, i.e., not well constrained. According to this, we used a simplified version of the FHT interaction where the central V_c^{10}, V_c^{01}, and tensor V_T^{10} terms have been considered. This choice is also justified by the Effective Field Theory (EFT) arguments [118, 119, 120, 121, 122]. Indeed, in the EFT expansion of the bare nucleon-nucleon interaction, these three terms appear at leading order, whereas the other terms present in the original FHT interaction correspond to higher orders of EFT. However, we have observed that adding the central term V_c^{00} improves the overall description of the nuclei considered in this work and hence we have also included it in $V_{i,j}$.

As it is customary in shell model studies [123, 124], a mass-dependent interaction-scaling factor of the form $(6/A)^\alpha$ is introduced to effectively account for the missing three-body forces [125, 126]. We found that the value $\alpha = 1/3$ gives a very reasonable description of experimental energies.

Finally, the Coulomb interaction between valence protons is treated by incorporating its long-range part into the basis potential and expanding the short-range two-body component in a truncated basis of HO states [127, 128].

4.2.2 Interaction optimization

The parameters (or even the form) of the effective nuclear interaction are not defined unambiguously. They can vary in different regions of the nuclear chart when considering in-medium effects. In order to provide predictions, the interaction parameters have been optimized through a fitting process, which consists in the minimization of the χ^2 penalty function

$$\chi^2(\boldsymbol{p}) = \sum_{i=1}^{N_d} \left(\frac{\mathcal{O}_i(\boldsymbol{p}) - \mathcal{O}_i^{\mathrm{exp}}}{\delta \mathcal{O}_i} \right)^2, \tag{4.7}$$

where N_d is the number of observables and $\boldsymbol{p}$ is a vector of parameter used. $\mathcal{O}(\boldsymbol{p})$ and $\mathcal{O}_i^{\mathrm{exp}}$ are the calculated value for observables and experimental values, respectively. $\delta\mathcal{O}_i$ is the adopted error that has been estimated by normalizing the penalty function to the number of degrees of freedom $N_{dof} = N_d - N_p$ at the minimum $\chi^2(\boldsymbol{p}_0)$ [129]. In the case of a single type of data and assuming that experimental and numerical errors are negligible, this can be achieved through a global scaling of the initial adopted errors $\delta\mathcal{O}_i \rightarrow \delta\mathcal{O}_i\sqrt{\chi^2(\boldsymbol{p_0})/N_{\mathrm{dof}}}$ [110]. This renormalization guarantees that $\chi^2 \sim 1$, which is necessary for calculated statistical uncertainties to be meaningful [130].

Interactions used in this model are linear in strength parameters, which enables us to calculate the first derivative (Jacobian J) exactly using Hellmann-Feynman theorem [131],

$$J_{i\alpha} = \frac{1}{\delta\mathcal{O}_i} \left. \frac{\partial \mathcal{O}_i}{\partial p_\alpha} \right|_{\boldsymbol{p}_0} . \tag{4.8}$$

The covariance matrix $\mathcal{C}$ can be approximately expressed in terms of Jacobian J:

$$\mathcal{C} \simeq (J^T J)^{-1} \tag{4.9}$$

The uncertainty for each parameter is given by the diagonal elements in the covariance matrix $\mathcal{C}$, and the correlation between parameters α and β is given by [110]

$$c_{\alpha\beta} = \frac{\mathcal{C}_{\alpha\beta}}{\sqrt{C_{\alpha\alpha} C_{\beta\beta}}}. \tag{4.10}$$

In the situation where the Jacobian matrix is noninvertible or has a very small determinant, the Gauss-Newton method used in the minimization of χ^2 becomes unstable as the Jacobian matrix must be inverted. This typically happens when some parameters are sloppy, i.e., not well constrained by observables. To stabilize the calculation, the matrix inversion is replaced by its pseudo-inverse, derived from the singular value decomposition (SVD) of the Jacobian matrix [110].

The four strengths of the WS potential and four parameters of the two-body interaction are simultaneously optimized to reproduce fifteen energy levels of lithium isotopes and their mirror partners.

4.2.3 Model space

The calculations were performed in a model space which includes $s_{1/2}$, $p_{3/2}$ and $p_{1/2}$ partial waves for both protons and neutrons. Since the optimization involved energies only, for the sake of speeding-up the optimization and for better stability, we used a deeper WS potential to generate the basis, in which the $0p_{3/2}$ and $0p_{1/2}$ poles are bound. A real contour was then used to describe the non-resonant continuum space. The contour $\mathcal{L}^+$

for Berggren basis was divided into 3 segments with $k_{\text{peak}} = 0.25\,\text{fm}^{-1}$, $k_{\text{mid}} = 0.5\,\text{fm}^{-1}$, and the cutoff momentum $k_{\text{max}} = 4\,\text{fm}^{-1}$. Discretizing each segment with 10 points using the Gauss-Legendre quadrature guaranteed the convergence of results.

To calculate resonance's width, one has to generate a basis based on a much shallower basis-generating WS potential, in which the $0p_{3/2}$ and $0p_{1/2}$ poles are decaying resonances. In this case, a complex contour defined by a complex value of k_{peak} is employed. It is to be noted that the calculation of the width is more demanding than that of energy. A higher discretization of (20,20,20) is needed for the contour. Due to the Coulomb repulsion, the mean-field used to generate the s.p. basis for proton-rich nuclei varies with proton number. The contour was adjusted separately for each system to assure that the Berggren completeness relation is met. To ensure the numerical stability, the chosen contour should neither lie too close to the Gamow poles nor lie too far from the real-k axis. In this work, k_{peak} is chosen to lie slightly $(0.05\,\text{fm}^{-1})$ below the position of the $0p_{3/2}$, $0p_{1/2}$ poles, but with the imaginary part greater than $-0.2\,\text{fm}^{-1}$. The calculations were repeated with several slightly different values of k_{peak} to assure the full convergence of results.

As in any configuration interaction models, the dimension of the Hamiltonian matrix grows quickly with the number of active particles. In the context of the GSM, it increases more quickly than in the conventional shell model due to the presence of discretized scattering states. To this end, we truncated the model space by working with natural orbitals which provides an optimized set of s.p. states [110, 132, 133]. The natural orbitals are defined as the eigenvectors of the one-body density matrix [133], and have widely used in no-core shell model [134]. In this work, natural orbitals are first calculated in a truncated configuration space which permits only three valence particles in the continuum shells. A truncation is then performed on the s.p. basis by keeping only natural orbitals for which the modulus of the occupation number is greater than a certain value (10^{-6}). Finally, a new set of Slater determinants was constructed and served as the basis for the diagonalization of the Hamiltonian matrix using the Davidson method [135].

To check the accuracy of this truncation procedure in the case of the largest systems, computation of the energy was also performed using the Density Matrix Renormalization Group (DMRG) method [136, 137]. The DMRG allows performing calculations without truncation on the s.p. basis and without restrictions on the number of particles in the continuum. In this approach, the many-body Schrödinger equation was solved iteratively in tractable truncated spaces which were increased until numerical convergence was reached. We have checked that, in all cases discussed in this work, the GSM results were in good agreement with those of DMRG.

4.3 Results

4.3.1 Optimized states

To optimize our interaction, we used experimentally well-established levels, shown in Table 4.1 and marked with ★ in Figs. 4.1 and 4.2 respectively.

Table 4.1: Energy levels used in the GSM Hamiltonian optimization. The energies are given with respect to the ^{4}He g.s.. The experimental values E_{exp} are taken from Ref. [7]. They are compared to the GSM values E_{GSM}.

Nucleus	State	E_{exp} (MeV)	E_{GSM} (MeV)	Nucleus	State	E_{exp} (MeV)	E_{GSM} (MeV)
^{6}Li	1+	-3.70	-3.72				
	0+	-0.14	-0.10				
^{7}Li	3/2-	-10.95	-11.02	^{7}Be	3/2-	-9.30	-9.36
	1/2-	-10.47	-10.14		1/2-	-8.88	-8.53
^{8}Li	2+	-12.98	-13.14	^{8}B	2+	-9.44	-9.60
	1+	-12.00	-11.93		1+	-8.67	-8.50
^{9}Li	3/2-	-17.05	-16.90	^{9}C	3/2-	-10.74	-10.85
	1/2-	-14.35	-14.50		1/2-	-8.52	-8.59
^{11}Li	3/2-	-17.41	-17.48				

The experimental data are taken from Ref. [7] unless otherwise specified. All energies are considered relative to the g.s. energy of ^{4}He.

As can be seen in Table 4.1, very good consistency with experimental results has been achieved for the fifteen selected states. The rms deviation from experimental values is 160 keV. The largest discrepancy is obtained for the $1/2^-$ states of ^{7}Li and ^{7}Be, with a deviation of 340 keV from the data. All other states are within the range of 170 keV from experiment.

We also want to point out that three states lying close to the threshold are also well reproduced, including: (i) the 0^+ state of ^{6}Li which is 140 keV below the threshold of ^{4}He+n+p; (ii) the g.s. of halo nucleus ^{11}Li lying 369 keV below the two-neutron emission threshold; (iii) and the 2^+ state of ^{8}B being 140 keV away from one proton decay.

4.3.2 Optimized Interaction

The optimized values of the parameters for the WS potentials and the two-body interaction are displayed, along with their statistical uncertainties, in Tables 4.2 and 4.4, respectively. As one can judge from the small parameter uncertainties in Tables 4.2 and 4.4, the GSM Hamiltonian is rather well constrained. As expected, the central term V_c^{00} has the largest uncertainty of $\sim$12%.

Table 4.2: Central and spin-orbit strengths of the core-nucleon WS potential optimized in this work. The statistical uncertainties are given in parentheses.

Parameter	Neutrons	Protons
V_0 (MeV)	39.5 (2)	42.1 (4)
$V_{\ell s}$ (MeV·fm^2)	10.7 (2)	11.1 (5)

Compared with the core-nucleon potential parameters obtained by fitting proton-^{4}He and neutron-^{4}He phase shifts in Ref. [110], the strength parameter of core potentials for both protons and neutrons are shallower, which push p-shell poles up further into the continuum. Moreover, the spin-orbit strength is larger than that in Ref. [110], which separates the $0p_{3/2}$ and $0p_{1/2}$ poles further apart. Consequently, the $0p_{3/2}$ pole appears at similar energy as in Ref. [110] and the $0p_{1/2}$ pole lies high above in the

Table 4.3: Groud state energies (in MeV) and widths (in keV) of ^{5}He and ^{5}Li obtained from the optimized core-nucleon potential and compared to experiments [8, 9].

Nucleus	E_{GSM}	E_{exp}	Γ_{GSM}	Γ_{exp}
^{5}He	0.74	0.798	640	648
^{5}Li	1.6	1.69	1300	1230

Table 4.4: Strengths V_η^{ST} of the two-body interaction optimized in this work. The statistical uncertainties are given in parentheses.

parameter	value
V_c^{01} (MeV)	-9.425 (70)
V_c^{10} (MeV)	-8.309 (90)
V_c^{00} (MeV)	-8.895 (1130)
V_T^{10} (MeV$\cdot$fm^{-2})	-22.418 (970)

continuum. To assess the quality of the newly obtained interaction, the energy and width for the g.s. $(3/2^-)$ of both ^{5}He and ^{5}Li are calculated and shown in Table 4.3. These values are indeed very close to the experimental values.

The new core potential is not optimal in describing $0p_{1/2}$ resonant states of ^{5}He and ^{5}Li, whose physical importance decrease with its large decaying width. But this does not extend to heavier nuclei. For example, the $1/2^-$ state of ^{7}Li and ^{7}Be are mainly determined by the $0p_{1/2}$ pole and the obtained results are still quite close to the experimental data.

4.3.3 Test against other excited states

To check the quality of our optimized interaction, states not included in the optimization were calculated and compared with experiment. Results are shown in Figs. 4.1 and 4.2. To distinguish from the states used for optimization, states not entering the optimization are shown together with their energies displayed; the widths are marked by the shaded boxes.

The corresponding energies and statistical uncertainties of predicted states are listed in Table 4.5. As one can see, the optimized interaction

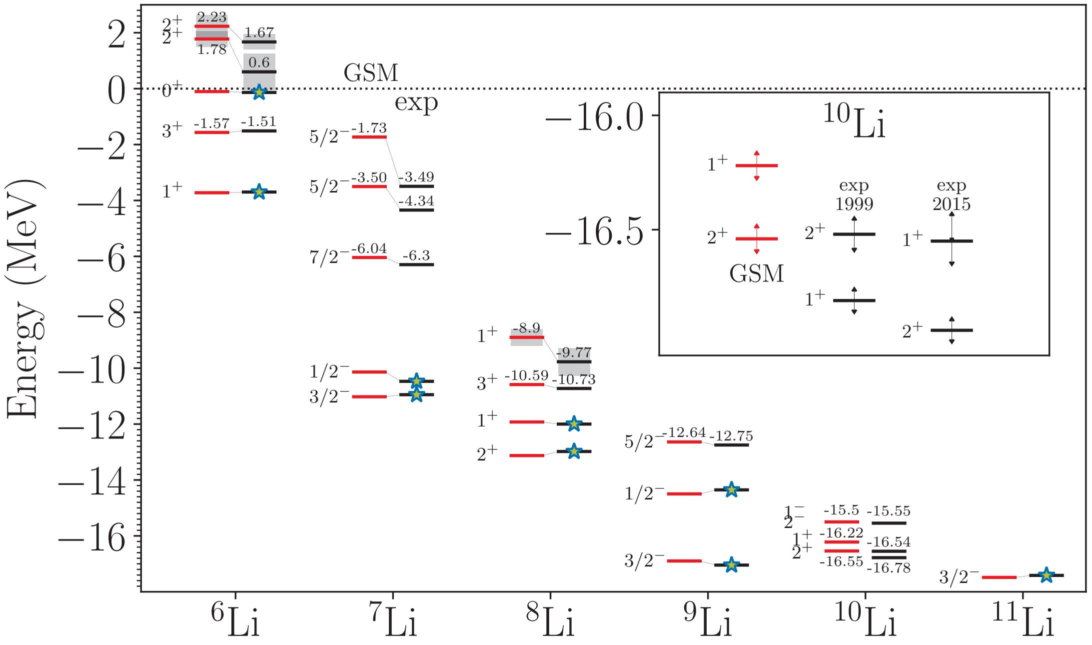

Figure 4.1: Energies for states of Li isotopes with respect to ^{4}He. Red lines denote GSM results and the black lines mark experimental values. The shaded area represents the width of the corresponding resonance. States used for optimization are marked with a ★, their energies are listed in Tables 4.1 and 4.5.

not only allows for a good reproduction of experimental energies for the fifteen selected states but also gives satisfactory results for excited states not included in the fit. For instance, the calculated 3^+ state in ^{6}Li at -1.57 MeV is only 60 keV below the experimental energy. The experimental widths for the second $5/2^-$ state in ^{7}Li (89 keV) and $5/2^-$ state in ^{9}Li (88 keV) are very reasonable: the calculated values are 22 and 62 keV, respectively.

The $5/2^-$ and $7/2-$ excited states in ^{7}Be are slightly (>300 keV) above the corresponding experimental values, whereas the position of the 3^+ state in ^{8}B and $5/2^-$ state in ^{9}C are well reproduced. It is also worth to mention that the second excited state $5/2^-$ of ^{9}C is in good consistency with the R-matrix analysis and continuum shell model calculations in Ref. [138]. The calculated width for $5/2^-$ state is 340 keV and very close to the value 673 ± 50 keV extracted from experiment [139].

Table 4.5: Energy levels for states not entering the optimization. The experimental values E_{exp} are taken from Ref. [7]. The GSM values E_{GSM} are shown with the uncertainties in parentheses.

Nucleus	State	E_{exp} (MeV)	E_{GSM} (MeV)	Nucleus	State	E_{exp} (MeV)	E_{GSM} (MeV)
^{6}Li	3^+	-1.51	-1.57(2)				
^{7}Li	$7/2^-$	-6.3	-6.04(2)	^{7}Be	$7/2^-$	-4.73	$-4.47(2)$
^{8}Li	3^+	-10.73	-10.59(2)	^{8}B	3^+	-7.12	-7.11(2)
^{9}Li	$5/2^-$	-12.75	-12.64(2)	^{9}C	$5/2^-$	-7.14	-7.12(5)
^{10}Li	2^+	-16.78	-16.55(5)	^{10}N	1^-	-8.84	-8.93(6)
	1^+	-16.54	-16.22(5)		2^-	-7.94	-8.46(6)

In general, we do not expect the same quality of data reproduction for all excited states due to the fact that the higher partial waves with

Table 4.6: Root-mean-square proton (R_p) and neutron (R_n) radii of ^{6}Li, ^{7}Li/^{7}Be, ^{8}Li/^{8}B, ^{9}Li/^{9}C, and ^{11}Li (in fm).

Nucleus	State	R_p/R_n(fm)	Nucleus	State	R_p/R_n(fm)
^{6}Li	1^+	2.22/2.21			
^{7}Li	$3/2^-$	2.12/2.28	^{7}Be	$3/2^-$	2.26/2.09
^{8}Li	2^+	2.12/2.48	^{8}B	2^+	2.57/2.14
^{9}Li	$3/2^-$	2.12/2.53	^{9}C	$3/2^-$	2.62/2.09
^{11}Li	$3/2^-$	2.12/2.81			

$\ell \geq 2$, which may contribute to the wave functions of those states, are not included in the model space. The estimated statistical uncertainties on the predicted energies are small: in most cases they are in the range of 20 – 60 keV.

4.3.4 Root-mean-square radius

One of the key features to identify halo nucleus is the rms radius. To give an estimation, Table 4.6 shows rms proton/neutron radius for lithium isotopes and their mirror partners [140]:

$$< r^2 >= \frac{2}{N_{\text{val}} + 2} < r^2_{\text{core}} > + \frac{N_{\text{val}}}{N_{\text{val}} + 2} < r_i^2 >, \qquad (4.11)$$

where the first and second term corresponds to the contribution from both the core and valence particles, respectively, with N_{val} being the number of valence protons/neutrons. The experimental value of 1.67 fm is used for the rms radius of both proton and neutron in the ^{4}He core [141]. Valence protons and neutrons are treated as point-like particles, whose sizes are not taken into account.

Since the corrections, such as spin-orbit effects and core swelling [140], are not included in our calculation, we do not intend to compare our results directly against to the experimental charge radii.

By comparing with other lithium isotopes, a dramatical increase of the rms neutron radius of ^{11}Li can be seen from Table 4.6, which indeed indicates the halo structure in ^{11}Li. Since all considered Li isotopes have only one well-bound valence proton, the proton radii are almost constant for each Li isotopes.

As to the proton-rich side, a sharp increment can be seen clearly for the rms proton radii for ^{8}B and ^{9}C as compared to those of ^{6}Li and ^{7}Be, suggesting that both ^{8}B and ^{9}C are indeed good candidates for proton halo nuclei due to their weakly bound properties [142, 143, 144].

4.3.5 Prediction for unbound nuclei: ^{10}Li, ^{10}N and ^{11}O

^{10}Li

Several experiments [43, 44, 45, 46] and theoretical calculations [145, 88] have indicated that the structure of the g.s. in ^{10}Li may correspond to a neutron in a virtual $\ell = 0$ state above a ^{9}Li core. However, the presence of such a virtual state near the threshold has not been confirmed in a recent experiment [146] with higher statistics, see the theoretical analysis [147, 148]. This indicates that the situation in ^{10}Li is still not well understood.

We wish to note, however, that a virtual state in ^{10}Li cannot be associated with an energy level of the system; the appearance of such a state in the complex-momentum plane manifests itself through a low-energy enhancement of the $n+^{9}$Li cross-section. For that reason, we lim-

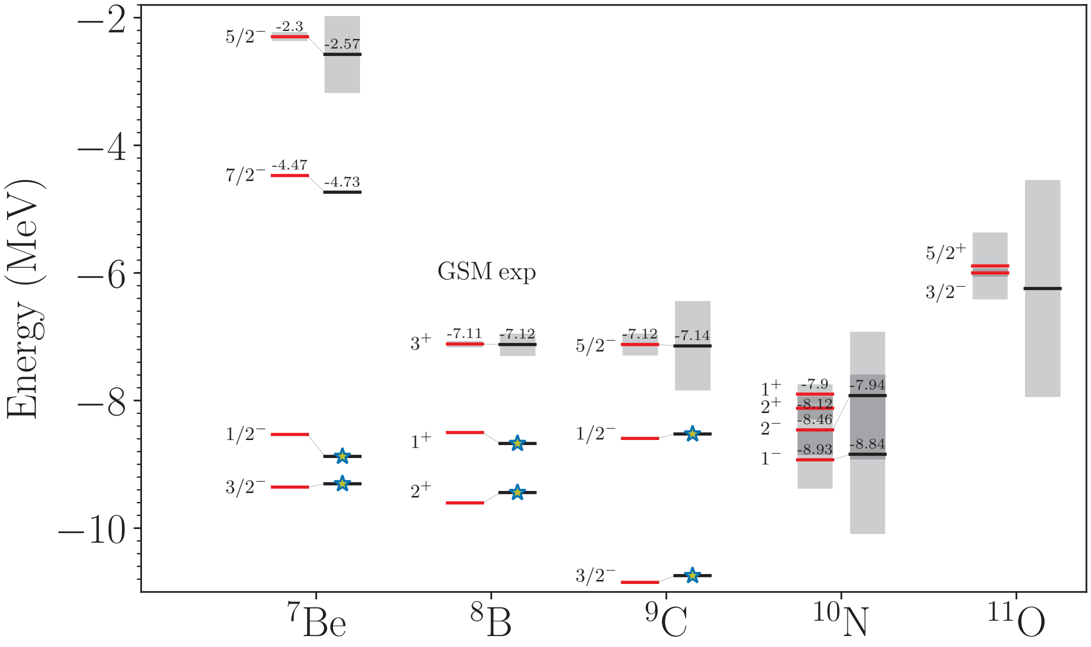

Figure 4.2: Similar to Fig. 4.1 for results of mirror nuclei of Li isotopes. Experimental energy of the $5/2^-$ resonance in ^{9}C was taken from Ref. [5] and the data for ^{11}O is from Ref. [6].

ited our calculations to resonant states in ^{10}Li that can be interpreted as experimentally-observable resonances.

The computed 2^+ g.s. and first excited state 1^+ of ^{10}Li lie at 0.35 and 0.68 MeV above the n+^{9}Li threshold, respectively. The next excited states are the degenerate 1^- and 2^- states at 1.05 MeV. Due to the strong coupling to the continuum in these states, using the WS potential of the GSM Hamiltonian to generate the basis would make the numerical computation unstable. To achieve the numerical stability, the computations were performed by a deeper WS potential. We have checked that our predicted energies do not depend on the choice of the WS used for the construction of the basis: in all cases considered, the variation of the energy did not exceed 1 keV. On the other hand, the computed width associated with the states is of the order of a few hundred keV and consequently not stable. For that reason, we do not show them in Fig. 4.1.

To shed light on the structure of ^{10}Li, Table 4.7 lists the squared amplitudes of the dominant neutron configurations for the four low-lying states of ^{10}Li. The positive parity states are primarily made from the $0p_{3/2}$ and $0p_{1/2}$ resonant shells. The negative parity states contain one neutron in the $1s_{1/2}$ shell. The contribution from the non-resonant continuum space to the low-lying states is very small.

Experimentally, Ref. [149] observed two positive-parity states at 0.24 MeV and 0.53 MeV above the n+^{9}Li threshold [149], with the lower state assigned to be 1^+. This spin assignment contradicts the results in Ref. [150] where the lowest positive parity state was assigned to be a 2^+, see the

Table 4.7: Squared amplitudes of dominant configuration of valence neutrons and protons for low-lying levels of ^{10}Li and ^{10}N, respectively. The odd proton in ^{10}Li and the odd neutron in ^{10}N occupy the $0p_{3/2}$ Gamow state. The tilde sign labels non-resonant continuum components.

configuration	^{10}Li		^{10}N	
	2^+	1^+	2^+	1^+
$(0p_{3/2})^4(0p_{1/2})^1$	0.84	0.81	0.81	0.78
$(0p_{3/2})^3(0p_{1/2})^2$	0.10	0.06	0.10	0.05
	1^-	2^-	1^-	2^-
$(0p_{3/2})^4(1s_{1/2})^1$	0.72	0.73	0.44	0.37
$(0p_{3/2})^4(\widetilde{s_{1/2}})^1$			0.29	0.35
$(0p_{3/2})^3(0p_{1/2})^1(1s_{1/2})^1$	0.14	0.14	0.09	0.07
$(0p_{3/2})^3(0p_{1/2})^1(\widetilde{s_{1/2}})^1$			0.06	0.07
$(0p_{3/2})^2(0p_{1/2})^2(1s_{1/2})^1$	0.07	0.07	0.04	0.03
$(0p_{3/2})^2(0p_{1/2})^2(\widetilde{s_{1/2}})^1$			0.03	0.03

inset in Fig. 4.1. In our prediction, the computed position of 1^-, 2^- are in agreement with the observation of a negative-parity state at 1.05 MeV from Ref. [146].

Unbound ^{10}N

^{10}N is the unbound mirror partner of ^{10}Li, lying beyond proton dripline. The spectrum of ^{10}N is not experimentally known with certainty. In Fig. 4.2, we show the tentative level assignments used in Ref. [7]. According to Refs. [151, 152], the g.s. of ^{10}N is most likely a 1^- state in the energy range from 1.81 to 1.94 MeV. In a more recent work [153], they observed two low-lying negative-parity states but they were not able to assign J^π values.

Due to the presence of the Coulomb barrier, the $1s_{1/2}$ single-proton state is a broad resonance rather than a virtual state [6, 154]. To capture this state, a complex contour is used with $k_{\text{peak}} = (0.25, -0.05)$ fm^{-1}. Our calculations for ^{10}N predict the g.s. to be a 1^- state with $(E, \Gamma) = (-8.93,\ 0.9)$ MeV that lies 1.92 MeV above the $1p$ threshold. The first excited state is predicted to be a 2^- state with $\Gamma = 0.3$ MeV slightly below the value quoted in Ref. [153]. This result is consistent with the recent Gamow coupled-channel analysis of Ref. [154]. We also predict an excited 1^+ state with Γ=0.3 MeV, lying 2.9 MeV above the ^{9}C+p threshold, which is consistent with Refs. [155, 156, 157]. A second positive-parity state with $J^\pi = 2^+$ is also predicted at 0.81 MeV with a width of 0.36 MeV.

Table 4.7 shows the squared amplitudes of the dominant proton configurations for the four low-lying states of ^{10}N. Similar to ^{10}Li, the positive parity states are primarily made from the $0p_{3/2}$ and $0p_{1/2}$ resonant shells. The dominant configurations of negative parity states contain one $\ell = 0$ proton, which can either be in the $1s_{1/2}$ shell or in a non-resonant continuum state.

Unbound ^{11}O

^{11}O is a $2p$-emitter as the mirror partner of the $2n$-halo nucleus ^{11}Li. With one more proton above ^{10}N, ^{11}O is more unbound, which makes it more challenging to study experimentally. The first observation of ^{11}O was done recently with two-neutron knockout reactions of ^{13}O beams at NSCL [6]. A broad peak with a width of 3.4 MeV was observed which was interpreted in terms of four overlapping resonances:$J^\pi = 3/2^-_1, 3/2^-_2, 5/2^+_1, 5/2^+_2$ [6, 154]. The $3/2_1^-$ and $5/2_1^+$ states are 4.16 MeV and 4.65 MeV above ^{9}C+2p threshold and the widths are 1.3 MeV and 1.06 MeV respectively.

In this work, we predicted the g.s. $3/2_1^-$ at 4.85 MeV with a width of 0.13 MeV and a first excited state $5/2_1^+$ at 5.03 MeV with the width of about 1 MeV. These predictions are consistent with the Gamow coupled-channel calculations of Refs. [6, 154].

4.3.6 Continuum effects on the Thomas-Ehrman shift

The Thomas-Ehrman shift [107, 108] reflects the energy shift between the mirror pair of nuclei primarily due to the Coulomb repulsion. To study the effect of particle continuum due to different positions of particle thresholds in mirror partners, we compared the level schemes of Li isotopes and their mirror partners with mass number $A = 7, 8, 9, 10$, from well-bound states to unbound resonances high above the threshold. Results are shown in Fig. 4.3. Within each pair, the ground states agree.

This agreement holds for excited states as long as both are bound, as can be seen for the $3/2^-$,$1/2^-$ and $7/2^-$ states of $A = 7$ nuclei in Fig. 4.3(a). Moving up to higher energy, the $5/2^-$ state of ^{7}Li and ^{7}Be are both above the one-nucleon emission threshold. The $5/2^-$ level of proton-rich nuclei ^{7}Be is lower than that of the neutron-rich partner ^{7}Li.

A similar trend can also be seen in results for the ^{8}Li/^{8}B and ^{9}Li/^{9}C pairs in Fig. 4.3(b,c). As discussed in Sec. 4.3.4, ^{8}B and ^{9}C are both likely to be halo nuclei having large spatial extensions.

The ^{10}Li/^{10}N pair is the most interesting one as both nuclei lie above

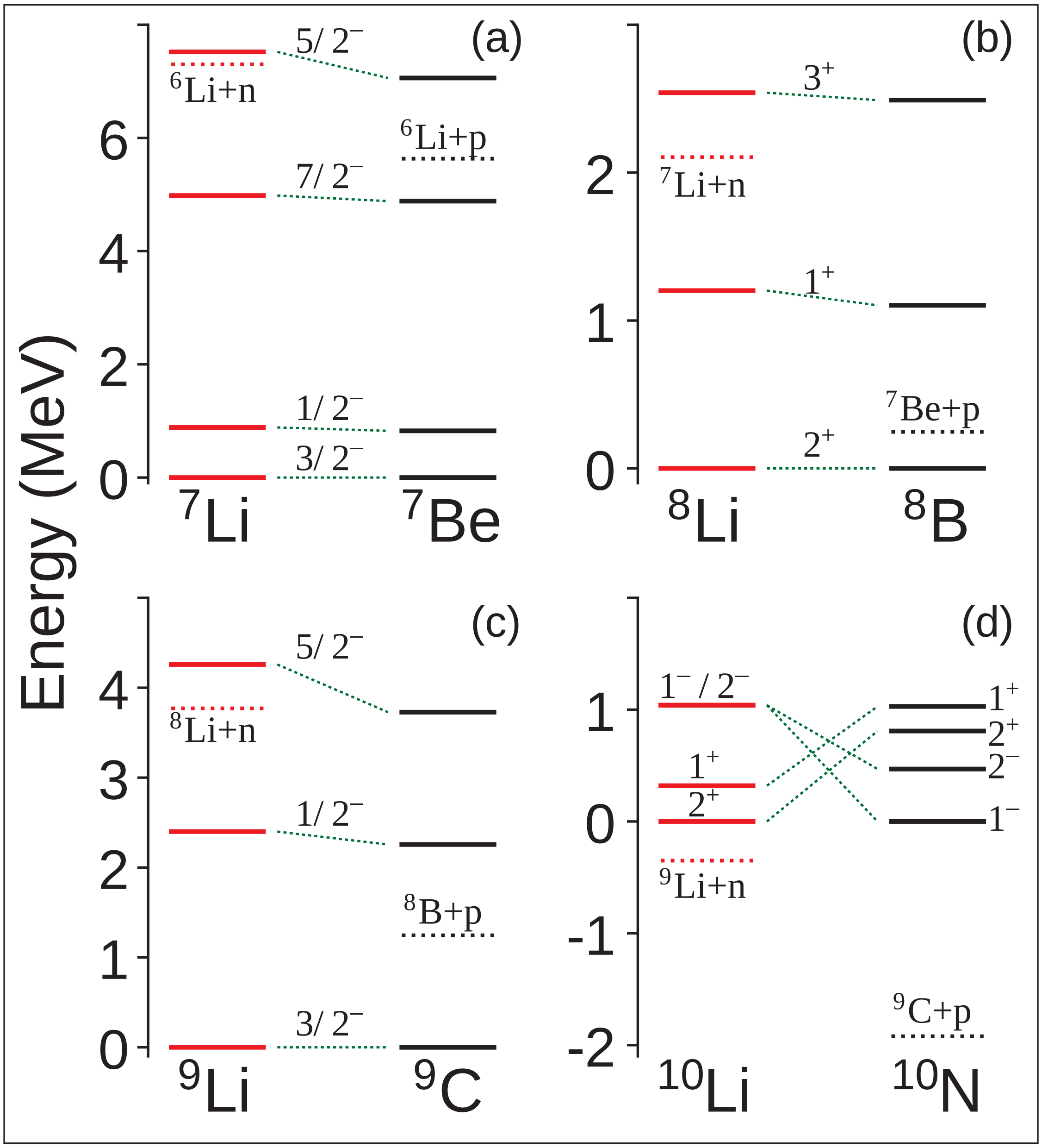

Figure 4.3: Spectrum for Li isotopes and their mirror partner with mass (a) $A = 7$, (b) $A = 8$, (c) $A = 9$, (d) $A = 10$. Within each pair, the spectrum of Li isotope and its mirror are plotted whin the same scale and different range. The plots are shifted so that the g.s. of each pair align with each other. The one-proton/neutron emission thresholds are also marked within each plot.

the particle threshold. As seen in Table 4.7, the effect of the very low ^{9}C+p threshold in ^{10}N on the negative-parity states 1^{-} and 2^{-} containing the s-wave proton is huge: it results in a rather dramatic shift of both negative parity states when going from ^{10}Li to ^{10}N that gives rise to a different structure of low-lying resonances in these nuclei.

Chapter 5

Conclusion and Outlook

This thesis is devoted to the study of OQSs with the complex-energy methods and proper description of continuum coupling. By studying both atomic anions and lithium isotopes (including their mirror partners), this work addresses important problems in the field of OQSs in atomic physics and nuclear physics.

In the atomic domain, quadrupolar anions and anions bounded by the multipolar Gaussian potentials were simulated using the complex-energy electron-plus-molecule model. The coupling between the rotational motion of the molecule and the valence electron near the dissociation threshold has been studied. By analyzing the rotational bands extended above the dissociation threshold, we predicted that spatial charge distribution does not affect the coupling between the molecule's rotational motion and electron's motion.

As for anions bounded by multipolar Gaussian potential, effects of the low-ℓ channels on the trajectory of resonant states in the complex-momentum plane are revealed. By increasing potential strength, a resonance with a moderate contribution from s-wave can become a subthreshold resonance, and then an antibound state that eventually becomes a bound state. This demonstrates that antibound states and subthreshold resonances, which can not be observed in experiments, can profoundly affect the structure of OQSs.

In the nuclear physics area, the properties of lithium isotopes and their mirror partners have been studied with an optimized FHT interaction. This interaction has been developed by fitting energies to fifteen well-established states of lithium isotopes and their mirror partners, with an rms deviation from experiments of 160 keV. Statistical analysis of the interaction parameters indicates the statistical uncertainty less than 12%. Calculations for other excited states demonstrate the good predictive power of the new interaction. Predictions have been make for the spectra of very exotic nuclei ^{10}Li, ^{10}N and ^{11}O. A very large Thomas-Ehrmann effect has been predicted for ^{10}Li/^{10}N pair.

In summary, in this work I applied the complex-energy method to study OQSs, from the simple one-body system (atomic anions) to the complicated many-body systems (lithium isotopes and their mirror partners). We intend to extend this work to other isotopic chains such as boron and beryllium isotopes. Other anticipated applications include two-nucleon radioactivity, clustering and isospin violation in dripline nuclei.

Chapter 6

List of Publications

1. K. Fossez , **X. Mao**, W. Nazarewicz, N. Michel, W. R. Garrett, and M. Płoszajczak. Resonant spectra of quadrupolar anions. *Phys. Rev. A*, 94:032511, 2016.
    - Performed the calculation for rotational bands.
    - Contributed to the rotational bands part of the draft.
2. **X. Mao**, K. Fossez, W. Nazarewicz. Resonant spectra of multipole-bound anions. *Phys. Rev. A*, 98:062515, 2018.
    - Developed a C++ code for the Gaussian potential part.
    - Performed the calculations, analyzed results, and produced figures.
    - Wrote the first draft of the manuscript.
3. **X.Mao**, J.Rotureau, W.Nazarewicz. Gamow shell model description of Li isotopes and their mirror partners. arXiv:2004.02981, 2020
    - Carried out all the calculations, including the interaction optimization and GSM studies of individual nuclei .

- Developed Python scripts to generate all the plots.
- Selected experimental data and researched literature.
- Wrote the first draft of the manuscript.

Bibliography

[1] N. Michel, W. Nazarewicz, M. Płoszajczak, and T. Vertse. Shell model in the complex energy plane. *J. Phys. G*, 36:013101, 2009.

[2] X. Mao, K. Fossez, and W. Nazarewicz. Resonant spectra of multipole-bound anions. *Phys. Rev. A*, 98:062515, 2018.

[3] W. R. Garrett. Critical electron binding to linear electric quadrupole systems. *J. Chem. Phys.*, 128:194309, 2008.

[4] K. Fossez, X. Mao, W. Nazarewicz, N. Michel, W. R. Garrett, and M. Płoszajczak. Resonant spectra of quadrupolar anions. *Phys. Rev. A*, 94:032511, 2016.

[5] G. V. Rogachev, J. J. Kolata, A. S. Volya, F. D. Becchetti, Y. Chen, P. A. DeYoung, and J. Lupton. Spectroscopy of ^{9}C via resonance scattering of protons on ^{8}B. *Phys. Rev. C*, 75:014603, 2007.

[6] T. B. Webb, S. M. Wang, K. W. Brown, R. J. Charity, J. M. Elson, J. Barney, G. Cerizza, Z. Chajecki, J. Estee, D. E. M. Hoff, S. A. Kuvin, W. G. Lynch, J. Manfredi, D. McNeel, P. Morfouace, W. Nazarewicz, C. D. Pruitt, C. Santamaria, J. Smith, L. G. Sobotka, S. Sweany, C. Y. Tsang, M. B. Tsang, A. H. Wuosmaa,

Y. Zhang, and K. Zhu. First observation of unbound ^{11}O, the mirror of the halo nucleus ^{11}Li. *Phys. Rev. Lett.*, 122:122501, 2019.

[7] `http://www.nndc.bnl.gov/ensdf`, 2015.

[8] D. R. Tilley, C. M. Cheves, J. L. Godwin, G. M. Hale, H. M. Hofmann, J. H. Kelley, C. G. Sheu, and H. R. Weller. Energy levels of light nuclei $A = 5, 6, 7$. *Nucl. Phys. A*, 708:3, 2002.

[9] `http://www.tunl.duke.edu/nucldata/`, 2015.

[10] T. Berggren. On the use of resonant states in eigenfunction expansions of scattering and reaction amplitudes. *Nucl. Phys. A*, 109:265, 1968.

[11] A. B. Balantekin, J. Carlson, D. J. Dean, G. M. Fuller, R. J. Furnstahl, M. Hjorth-Jensen, R. V. F. Janssens, Bao-An Li, W. Nazarewicz, F. M. Nunes, and W. E. Ormand. *Mod. Phys. Lett. A*, 29:1430010, 2014.

[12] J. Al-Khalili. *An Introduction to Halo Nuclei.* Springer Berlin Heidelberg, Berlin, Heidelberg, 2004.

[13] K. Riisager. Nuclear halo states. *Rev. Mod. Phys.*, 66:1105, 1994.

[14] A. S. Jensen, K. Riisager, D. V. Fedorov, and E. Garrido. Structure and reactions of quantum halos. *Rev. Mod. Phys.*, 76:215, 2004.

[15] V. Tripathi, S. L. Tabor, P. F. Mantica, C. R. Hoffman, M. Wiedeking, A. D. Davies, S. N. Liddick, W. F. Mueller, T. Otsuka, A. Stolz,

B. E. Tomlin, Y. Utsuno, and A. Volya. ^{29}Na: Defining the edge of the island of inversion for $Z = 11$. *Phys. Rev. Lett.*, 94:162501, 2005.

[16] Y. Kondo, T. Nakamura, R. Tanaka, R. Minakata, S. Ogoshi, N. A. Orr, N. L. Achouri, T. Aumann, H. Baba, F. Delaunay, P. Doomenbal, N. Fukuda, J. Gibelin, J. W. Hwang, N. Inabe, T. Isobe, D. Kameda, D. Kanno, S. Kim, N. Kobayashi, T. Kobayashi, T. Kubo, S. Leblond, J. Lee, F. M. Marqués, T. Motobayashi, D. Murai, T. Murakami, K. Muto, T. Nakashima, N. Nakatsuka, A. Navin, S. Nishi, H. Otsu, H. Sato, Y. Satou, Y. Shimizu, H. Suzuki, K. Takahashi, H. Takeda, S. Takeuchi, Y. Togano, A. G. Tuff, M. Vandebrouck, and K. Yoneda. Nucleus ^{26}O: A barely unbound system beyond the drip line. *Phys. Rev. Lett.*, 116:102503, 2016.

[17] J. S. Al-Khalili and J. A. Tostevin. Matter radii of light halo nuclei. *Phys. Rev. Lett.*, 76:3903, 1996.

[18] M. Freer. The clustered nucleus–cluster structures in stable and unstable nuclei. *Rep. Prog. Phys.*, 70:2149, 2007.

[19] M. Freer, H. Horiuchi, Y. Kanada-En'yo, D. Lee, and U. Meißner. Microscopic clustering in light nuclei. *Rev. Mod. Phys.*, 90:035004, 2018.

[20] C. Dossat, A. Bey, B. Blank, G. Canchel, A. Fleury, J. Giovinazzo, I. Matea, F. de Oliveira Santos, G. Georgiev, S. Grévy, I. Stefan, J. C. Thomas, N. Adimi, C. Borcea, D. Cortina Gil, M. Caamano, M. Stanoiu, F. Aksouh, B. A. Brown, and L. V. Grigorenko.

Two-proton radioactivity studies with ^{45}Fe and ^{48}Ni. *Phys. Rev. C*, 72:054315, 2005.

[21] B. Blank, A. Bey, G. Canchel, C. Dossat, A. Fleury, J. Giovinazzo, I. Matea, N. Adimi, F. De Oliveira, I. Stefan, G. Georgiev, S. Grévy, J. C. Thomas, C. Borcea, D. Cortina, M. Caamano, M. Stanoiu, F. Aksouh, B. A. Brown, F. C. Barker, and W. A. Richter. First observation of ^{54}Zn and its decay by two-proton emission. *Phys. Rev. Lett.*, 94:232501, 2005.

[22] J. Giovinazzo, B. Blank, M. Chartier, S. Czajkowski, A. Fleury, M. J. Lopez Jimenez, M. S. Pravikoff, J.-C. Thomas, F. de Oliveira Santos, M. Lewitowicz, V. Maslov, M. Stanoiu, R. Grzywacz, M. Pfützner, C. Borcea, and B. A. Brown. Two-proton radioactivity of ^{45}Fe. *Phys. Rev. Lett.*, 89:102501, 2002.

[23] B. Blank and M. Płoszajczak. Two-proton radioactivity. *Rep. Prog. Phys.*, 71:046301, 2008.

[24] I. Tanihata, H. Hamagaki, O. Hashimoto, Y. Shida, N. Yoshikawa, K. Sugimoto, O. Yamakawa, T. Kobayashi, and N. Takahashi. Measurements of interaction cross sections and nuclear radii in the light p-shell region. *Phys. Rev. Lett.*, 55:2676, 1985.

[25] D. L. Auton. Direct reactions on ^{10}Be. *Nucl. Phys. A*, 157:305, 1970.

[26] F. Ajzenberg-Selove, E. R. Flynn, and O. Hansen. (t,p) reactions on ^{4}He, ^{6}Li, ^{7}Li, ^{9}Be, ^{10}B, ^{11}B, and ^{12}C. *Phys. Rev. C*, 17:1283, 1978.

[27] R. Ringle, M. Brodeur, T. Brunner, S. Ettenauer, M. Smith, A. Lapierre, V.L. Ryjkov, P. Delheij, G.W.F. Drake, J. Lassen, D. Lunney, and J. Dilling. High-precision Penning trap mass measurements of ^{9,10}Be and the one-neutron halo nuclide ^{11}be. *Phys. Lett. B*, 675(2):170, 2009.

[28] H. Esbensen, B. A. Brown, and H. Sagawa. Positive parity states in ^{11}Be. *Phys. Rev. C*, 51:1274, 1995.

[29] M. V. Zhukov, B. V. Danilin, D. V. Fedorov, J. M. Bang, I. J. Thompson, and J. S. Vaagen. Bound state properties of Borromean halo nuclei: ^{6}He and ^{11}Li. *Phys. Rep.*, 231:151, 1993.

[30] G. Gamow. Zur Quantentheorie des Atomkernes. *Z. Physik*, 51:204, 1928.

[31] R. W. Gurney and E. U. Condon. Quantum mechanics and radioactive disintegration. *Phys. Rev.*, 33:127, 1929.

[32] A. F. J. Siegert. On the derivation of the dispersion formula for nuclear reactions. *Phys. Rev.*, 56:750, 1939.

[33] L. P. Kok. Accurate determination of the ground-state level of the ^{2}He nucleus. *Phys. Rev. Lett.*, 45:427, 1980.

[34] A. M. Mukhamedzhanov, B. F. Irgaziev, V. Z. Goldberg, Yu. V. Orlov, and I. Qazi. Bound, virtual, and resonance S-matrix poles from the Schrödinger equation. *Phys. Rev. C*, 81:054314, 2010.

[35] A. M. Mukhamedzhanov, Shubhchintak, and C. A. Bertulani. Subthreshold resonances and resonances in the R-matrix method for binary reactions and in the Tgrojan horse method. *Phys. Rev. C*, 96:024623, 2017.

[36] S. A. Sofianos, S. A. Rakityansky, and G. P. Vermaak. Subthreshold resonances in few-neutron systems. *J. Phys. G*, 23:1619, 1997.

[37] B. Gyarmati and T. Vertse. On the normalization of Gamow functions. *Nucl. Phys. A*, 160:523, 1971.

[38] B. Simon. The definition of molecular resonance curves by the method of exterior complex scaling. *Phys. Lett. A*, 71:211, 1979.

[39] R. G. Newton. *Scattering Theory of Waves and Particles.* Springer-Verlag, New York, 2nd edition, 1982.

[40] H. M. Nussenzveig. *Causality and Dispersion Relations.* Academic, New York, 1st edition, 1972.

[41] J. R. Taylor. *Scattering Theory: The Quantum Theory on Nonrelativistic Collisions.* John Wiley and Sons, Inc., New York, 1st edition, 1972.

[42] W. Domcke. Analytic theory of resonances, virtual states and bound states in electron-molecule scattering and related processes. *J. Phys. B*, 14:4889, 1981.

[43] M. Zinser, F. Humbert, T. Nilsson, W. Schwab, Th. Blaich, M. J. G. Borge, L. V. Chulkov, H. Eickhoff, Th. W. Elze, H. Emling,

B. Franzke, H. Freiesleben, H. Geissel, K. Grimm, D. Guillemaud-Mueller, P. G. Hansen, R. Holzmann, H. Irnich, B. Jonson, J. G. Keller, O. Klepper, H. Klingler, J. V. Kratz, R. Kulessa, D. Lambrecht, Y. Leifels, A. Magel, M. Mohar, A. C. Mueller, G. Münzenberg, F. Nickel, G. Nyman, A. Richter, K. Riisager, C. Scheidenberger, G. Schrieder, B. M. Sherrill, H. Simon, K. Stelzer, J. Stroth, O. Tengblad, W. Trautmann, E. Wajda, and E. Zude. Study of the unstable nucleus ^{10}Li in stripping reactions of the radioactive projectiles ^{11}Be and ^{11}Li. *Phys. Rev. Lett.*, 75:1719, 1995.

[44] M. Thoennessen, S. Yokoyama, A. Azhari, T. Baumann, J. A. Brown, A. Galonsky, P. G. Hansen, J. H. Kelley, R. A. Kryger, E. Ramakrishnan, and P. Thirolf. Population of ^{10}Li by fragmentation. *Phys. Rev. C*, 59:111, 1999.

[45] H.B. Jeppesen, A.M. Moro, U.C. Bergmann, M.J.G. Borge, J. Cederkäll, L.M. Fraile, H.O.U. Fynbo, J. Gómez-Camacho, H.T. Johansson, B. Jonson, M. Meister, T. Nilsson, G. Nyman, M. Pantea, K. Riisager, A. Richter, G. Schrieder, T. Sieber, O. Tengblad, E. Tengborn, M. Turrión, and F. Wenander. Study of ^{10}Li via the ^{9}Li(^{2}H,p) reaction at REX-ISOLDE. *Phys. Lett. B*, 642:449, 2006.

[46] H. Simon, M. Meister, T. Aumann, M.J.G. Borge, L.V. Chulkov, U. Datta Pramanik, Th.W. Elze, H. Emling, C. Forssén, H. Geissel, M. Hellström, B. Jonson, J.V. Kratz, R. Kulessa, Y. Leifels, K. Markenroth, G. Münzenberg, F. Nickel, T. Nilsson, G. Nyman, A. Richter, K. Riisager, C. Scheidenberger, G. Schrieder, O. Teng-

blad, and M.V. Zhukov. Systematic investigation of the drip-line nuclei ^{11}Li and ^{14}Be and their unbound subsystems ^{10}Li and ^{13}Be. *Nucl. Phys. A*, 791:267, 2007.

[47] E. Fermi and E. Teller. The capture of negative mesotrons in matter. *Phys. Rev.*, 72:399, 1947.

[48] J. E. Turner. Minimum dipole moment required to bind an electron – molecular theorists rediscover phenomenon mentioned in Fermi-Teller paper twenty years earlier. *Am. J. Phys.*, 45:758, 1977.

[49] T. Klahn and P. Krebs. Electron and anion mobility in low density hydrogen cyanide gas. I. Dipole-bound electron ground states. *J. Chem. Phys.*, 109:531, 1998.

[50] C. Desfrançois, H. Abdoul-Carime, and J. P. Schermann. Ground-state dipole-bound anions. *Int. J. Mol. Phys. B*, 10:1339, 1996.

[51] R. N. Compton and N. I. Hammer. *Multipole-Bound Molecular Anions*. Elsevier, 1st edition, 2001.

[52] K. D. Jordan and F. Wang. Theory of dipole-bound anions. *Annu. Rev. Phys. Chem.*, 54:367, 2003.

[53] J. Simons. Molecular anions. *J. Phys. Chem. A*, 112:6401, 2008.

[54] K. Fossez, N. Michel, W. Nazarewicz, M. Płoszajczak, and Y. Jaganathen. Bound and resonance states of the dipolar anion of hydrogen cyanide: Competition between threshold effects and rotation in an open quantum system. *Phys. Rev. A*, 91:012503, 2015.

[55] J. von Stecher, J. P. D'Incao, and C. H. Greene. Signatures of universal four-body phenomena and their relation to the Efimov effect. *Nature Phys.*, 5:417, 2009.

[56] M. R. Hadizadeh, M. T. Yamashita, Lauro Tomio, A. Delfino, and T. Frederico. Scaling properties of universal tetramers. *Phys. Rev. Lett.*, 107:135304, 2011.

[57] M. R. Hadizadeh, M. T. Yamashita, Lauro Tomio, A. Delfino, and T. Frederico. Universality and scaling limit of weakly-bound tetramers. *AIP Conf. Proc.*, 1423:130, 2012.

[58] R. Lazauskas and J. Carbonell. Complex scaling method for three- and four-body scattering above the break-up thresholds. *Few-Body Syst.*, 54:967, 2013.

[59] A. Kievsky, M. Gattobigio, and E. Garrido. Universality in few-body systems: from few-atoms to few-nucleons. *J. Phys. Conf. Ser.*, 527:012001, 2014.

[60] S. König, H. W. Grießhammer, H. W. Hammer, and U. van Kolck. Nuclear physics around the unitariry limit. *Phys. Rev. Lett.*, 118:202501, 2017.

[61] R. Álvarez-Rodríguez, A. Deltuva, M. Gattobigio, and A. Kievsky. Matching universal behavior with potential models. *Phys. Rev. A*, 93:062701, 2016.

[62] A. Deltuva. Universality in fermionic dimer-dimer scattering. *Phys. Rev. A*, 96:022701, 2017.

[63] M. A. Shalchi, M. T. Yamashita, M. R. Hadizadeh, T. Frederico, and Lauro Tomio. Neutron-^{19}C scattering: Emergence of universal properties in a finite range potential. *Phys. Lett. B*, 764:196, 2017.

[64] G. A. Miller. Non-universal and universal aspects of the large scattering length limit. *Phys. Lett. B*, 777:442, 2018.

[65] E. Braaten and H. W. Hammer. Universality in few-body systems with large scattering length. *Phys. Rep.*, 428:259, 2006.

[66] C. A. Bertulani, H. W. Hammer, and U. van Kolck. Effective field theory for halo nuclei: shallow *p*-wave states. *Nucl. Phys. A*, 712:37, 2002.

[67] P. F. Bedaque, H. W. Hammer, and U. van Kolck. Narrow resonances in effective field theory. *Phys. Lett. B*, 569:159, 2003.

[68] H. W. Hammer and L. Platter. Efimov states in nuclear and particle physics. *Annu. Rev. Nucl. Part. Sci.*, 60:207, 2010.

[69] H. W. Hammer and R. J. Furnstahl. Effective field theory for dilute Fermi systems. *Nucl. Phys. A*, 678:277, 2000.

[70] H. W. Hammer, C. Ji, and D. R. Phillips. Effective field theory description of halo nuclei. *J. Phys. G*, 44:103002, 2017.

[71] D. R. Herrick and P. C. Engelking. Dipole coupling channels for molecular anions. *Phys. Rev. A*, 29:2421, 1984.

[72] D. C. Clary. Photodetachment of electrons from dipolar anions. *J. Phys. Chem.*, 92:3173, 1988.

[73] D. C. Clary. Vibrationally induced photodetachment of electrons from negative molecular ions. *Phys. Rev. A*, 40:4392, 1989.

[74] E. A. Brinkman, S. Berger, J. Marks, and J. I. Brauman. Molecular rotation and the observation of dipole-bound states of anions. *J. Chem. Phys.*, 99:7586, 1993.

[75] S. Ard, W. R. Garrett, R. N. Compton, L. Adamowicz, and S. G. Stepanian. Rotational states of dipole-bound anions of hydrogen cyanide. *Chem. Phys. Lett.*, 473:223, 2009.

[76] W. R. Garrett. Non-Born-Oppenheimer approximation for very weakly bound states of molecular anions. *J. Chem. Phys.*, 133:224103, 2010.

[77] K. Fossez, N. Michel, W. Nazarewicz, and M. Płoszajczak. Bound states of dipolar molecules studied with the Berggren expansion method. *Phys. Rev. A*, 87:042515, 2013.

[78] A. Ferron, P. Serra, and S. Kais. Finite-size scaling for critical conditions for stable quadrupole-bound anions. *J. Chem. Phys.*, 120:8412, 2004.

[79] P. J. Linstrom and W. G. Mallard. *NIST Chemistry WebBook*. National Institute of Standards and Technology, Washington, 1st edition, 2016.

[80] H. Abdoul-Carime and C. Desfrançois. Electrons weakly bound to molecules by dipolar, quadrupolar or polarization forces. *Eur. Phys. J. D*, 2:149, 1998.

[81] H. Abdoul-Carime, J. P. Schermann, and C. Desfrançois. Multipole-bound molecuar negative ions. *Few-Body Syst.*, 31:183, 2002.

[82] W. R. Garrett. Quadrupole-bound anions: Efficacy of positive versus negative quadrupole moments. *J. Chem. Phys.*, 136:054116, 2012.

[83] J. P. Neirotti, P. Serra, and S. Kais. Electronic structure critical parameters from finite-size scaling. *Phys. Rev. Lett.*, 79:3142, 1997.

[84] V. I. Pupyshev and A. Y. Ermilov. Bound states of multipoles. *Int. J. Quant. Chem.*, 96:185, 2004.

[85] T. Misu, W. Nazarewicz, and S. Åberg. Deformed nuclear halos. *Nucl. Phys. A*, 614:44, 1997.

[86] K. Riisager, A. S. Jensen, and P. Møller. Two-body halos. *Nucl. Phys. A*, 548:393, 1992.

[87] K. Yoshida and K. Hagino. Role of low-l component in deformed wave functions near the continuum threshold. *Phys. Rev. C*, 72:064311, 2005.

[88] R. M. Id Betan, R. J. Liotta, N. Sandulescu, and T. Vertse. A shell model representation with antibound states. *Phys. Lett. B*, 584:48, 2004.

[89] N. Michel, W. Nazarewicz, M. Płoszajczak, and J. Rotureau. Antibound states and halo formation in the Gamow shell model. *Phys. Rev. C*, 74:054305, 2006.

[90] K. Rohr and F. Linder. Vibrational excitation in $e-$HCl collisions at low energies. *J. Phys. B: Atom. Molec. Phys.*, 8:200, 1975.

[91] K. Rohr and F. Linder. Vibrational excitation of polar molecules by electron impact I. Threshold resonances in HF and HCl. *J. Phys. B: Atom. Molec. Phys.*, 9:2521, 1976.

[92] K. Rohr. Interaction mechanismes and cross sections for the scattering of low-energy electrons from HBr. *J. Phys. B: Atom. Molec. Phys.*, 11:1849, 1978.

[93] W. D. Heiss and R. G. Nazmitdinov. Spectral singularities and zero energy bound states. *Eur. Phys. J. D.*, 63:369, 2011.

[94] W. D. Heiss. The physics of exceptional points. *J. Phys. A: Math. Theor.*, 45:444016, 2012.

[95] M. Müller and I. Rotter. Exceptional points in open quantum systems. *J. Phys. A*, 41:244018, 2008.

[96] J. Okołowicz and M. Płoszajczak. Exceptional points in the scattering continuum. *Phys. Rev. C*, 80:034619, 2009.

[97] S. Garmon, M. Gianfreda, and N. Hatano. Bound states, scattering states, and resonant states in $\mathcal{PT}$-symmetric open quantum systems. *Phys. Rev. A*, 92:022125, 2015.

[98] K. Fossez, W. Nazarewicz, Y. Jaganathen, N. Michel, and M. Płoszajczak. Nuclear rotation in the continuum. *Phys. Rev. C*, 93:011305(R), 2016.

[99] M.A.K. Lodhi. Cluster model wave function of ^{6}Li. *Nuclear Physics A*, 97:449, 1967.

[100] P. G. Roos, D. A. Goldberg, N. fS. Chant, R. Woody, and W. Reichart. The α-d and τ-t cluster structure of ^{6}Li. *Nucl. Phys. A*, 257:317, 1976.

[101] I. Tanihata, H. Hamagaki, O. Hashimoto, S. Nagamiya, Y. Shida, N. Yoshikawa, O. Yamakawa, K. Sugimoto, T. Kobayashi, D. E. Greiner, N. Takahashi, and Y. Nojiri. Measurements of interaction cross sections and radii of He isotopes. *Phys. Lett. B*, 160:380, 1985.

[102] R. Crespo, J. A. Tostevin, and I. J. Thompson. Structure signatures in proton scattering from ^{9,11}Li. *Phys. Rev. C*, 54:1867, 1996.

[103] S. N. Ershov, B. V. Danilin, J. S. Vaagen, A. A. Korsheninnikov, and I. J. Thompson. Structure of the ^{11}Li continuum from breakup on proton target. *Phys. Rev. C*, 70:054608, 2004.

[104] D. Baye, E. M. Tursunov, and P. Descouvemont. β decay of ^{11}Li into ^{9}Li and a deuteron within a three-body model. *Phys. Rev. C*, 74:064302, 2006.

[105] P. Descouvemont. Microscopic three-cluster study of light exotic nuclei. *Phys. Rev. C*, 99:064308, 2019.

[106] Y. Kikuchi, T. Myo, K. Katō, and K. Ikeda. Coulomb breakup reactions of ^{11}Li in the coupled-channel ^{9}Li+n+n model. *Phys. Rev. C*, 87:034606, 2013.

[107] J. B. Ehrman. On the displacement of corresponding energy levels of C^{13} and N^{13}. *Phys. Rev.*, 81:412, 1951.

[108] R. G. Thomas. An analysis ofthe energy levels of the mirror nuclei, C^{13} and N^{13}. *Phys. Rev.*, 88:1109, 1952.

[109] Y. Suzuki and K. Ikeda. Cluster-orbital shell model and its application to the He isotopes. *Phys. Rev. C*, 38:410, 1988.

[110] Y. Jaganathen, R. M. Id Betan, N. Michel, W. Nazarewicz, and M. Płoszajczak. Quantified Gamow shell model interaction for *psd*-shell nuclei. *Phys. Rev. C*, 96:054316, 2017.

[111] I. Sick. Precise root-mean-square radius of ^{4}He. *Phys. Rev. C*, 77:041302, 2008.

[112] H. Furutani, H. Horiuchi, and R. Tamagaki. Structure of the second 0^{+} state of ^{4}He. *Prog. Theor. Phys.*, 60:307, 1978.

[113] H. Furutani, H. Horiuchi, and R. Tamagaki. Cluster-model study of the $T = 1$ states in $A = 4$ system. *Prog. Theor. Phys.*, 62:981, 1979.

[114] K. Fossez, J. Rotureau, N. Michel, and W. Nazarewicz. Continuum effects in neutron-drip-line oxygen isotopes. *Phys. Rev. C*, 96:024308, 2017.

[115] K. Fossez, J. Rotureau, N. Michel, Q. Liu, and W. Nazarewicz. Single-particle and collective motion in unbound deformed ^{39}Mg. *Phys. Rev. C*, 94:054302, 2016.

[116] M. D. Jones, K. Fossez, T. Baumann, P. A. DeYoung, J. E. Finck, N. Frank, A. N. Kuchera, N. Michel, W. Nazarewicz, J. Rotureau, J. K. Smith, S. L. Stephenson, K. Stiefel, M. Thoennessen, and R. G. T. Zegers. Search for excited states in ^{25}O. *Phys. Rev. C*, 96:054322, 2017.

[117] K. Fossez, J. Rotureau, and W. Nazarewicz. Energy spectrum of neutron-rich helium isotopes: Complex made simple. *Phys. Rev. C*, 98:061302, 2018.

[118] C. Ordóñez and U. van Kolck. Chiral lagrangians and nuclear forces. *Phys. Lett. B*, 291:459, 1992.

[119] P. F. Bedaque and U. van Kolck. Effective field theory for few-nucleon systems. *Annu. Rev. Nucl. Part. Sci.*, 52:339, 2002.

[120] P. F. Bedaque, H. W. Hammer, and U. van Kolck. Narrow resonances in effective field theory. *Phys. Lett. B*, 569:159, 2003.

[121] I. Stetcu, J. Rotureau, B. R. Barrett, and U. van Kolck. Effective interactions for light nuclei: an effective (field theory) approach. *J. Phys. G*, 37:064033, 2010.

[122] P. Capel, V. Durant, L. Huth, H.-W. Hammer, D. R. Phillips, and A. Schwenk. From ab initio structure predictions to reaction calculations via EFT. *J. Phys.: Conf. Ser.*, 1023:012010, 2018.

[123] B. A. Brown and W. A. Richter. New "USD" Hamiltonians for the *sd* shell. *Phys. Rev. C*, 74:034315, 2006.

[124] L. Huth, V. Durant, J. Simonis, and A. Schwenk. Shell-model interactions from chiral effective field theory. *Phys. Rev. C*, 98:044301, 2018.

[125] A. P. Zuker. Three-body monopole corrections to realistic interactions. *Phys. Rev. Lett.*, 90:042502, 2003.

[126] S. R. Stroberg, H. Hergert, S. K. Bogner, and J. D. Holt. Nonempirical interactions for the nuclear shell model: An update. *Annu. Rev. Nucl. Part. S.*, 69:307, 2019.

[127] G. Hagen, M. Hjorth-Jensen, and N. Michel. Gamow shell model and realistic nucleon-nucleon interactions. *Phys. Rev. C*, 73:064307, 2006.

[128] N. Michel, W. Nazarewicz, and M. Płoszajczak. Isospin mixing and the continuum coupling in weakly bound nuclei. *Phys. Rev. C*, 82:044315, 2010.

[129] R. T. Birge. The calculation of errors by the method of least squares. *Phys. Rev.*, 40:207, 1932.

[130] J. Dobaczewski, W. Nazarewicz, and P.-G. Reinhard. Error estimates in theoretical models: A guide. *J. Phys. G*, 41:074001, 2014.

[131] R. P. Feynman. Forces in molecules. *Phys. Rev.*, 56:340, 1939.

[132] L. Brillouin. La méthode du champ self-consistent. *Act. Sci. Ind.*, 71:159, 1933.

[133] I. J. Shin, Y. Kim, P. Maris, J. P. Vary, C. Forssén, J. Rotureau, and N. Michel. *Ab initio* no-core solutions for ^{6}Li. *J. Phys. G*, 44:075103, 2017.

[134] Ch. Constantinou, M. A. Caprio, J. P. Vary, and P. Maris. Natural orbital description of the halo nucleus ^{6}He. *Nucl. Sci. Tech.*, 28:179, 2017.

[135] G. J. G. Sleijpen and H. A. van der Vorst. A Jacobi–Davidson iteration method for linear eigenvalue problems. *SIAM J. Matrix Anal. Appl.*, 17:401, 1996.

[136] J. Rotureau, N. Michel, W. Nazarewicz, M. Płoszajczak, and J. Dukelsky. Density matrix renormalisation group approach for many-body open quantum systems. *Phys. Rev. Lett.*, 97:110603, 2006.

[137] J. Rotureau, N. Michel, W. Nazarewicz, M. Płoszajczak, and J. Dukelsky. Density matrix renormalization group approach to two-fluid open many-fermion systems. *Phys. Rev. C*, 79:014304, 2009.

[138] G. V. Rogachev, J. J. Kolata, A. S. Volya, F. D. Becchetti, Y. Chen, P. A. DeYoung, and J. Lupton. Spectroscopy of ^{9}C via resonance scattering of protons on ^{8}B. *Phys. Rev. C*, 75:014603, 2007.

[139] K. W. Brown, R. J. Charity, J. M. Elson, W. Reviol, L. G. Sobotka, W. W. Buhro, Z. Chajecki, W. G. Lynch, J. Manfredi, R. Shane, R. H. Showalter, M. B. Tsang, D. Weisshaar, J. R. Winkelbauer, S. Bedoor, and A. H. Wuosmaa. Proton-decaying states in light nuclei and the first observation of ^{17}Na. *Phys. Rev. C*, 95:044326, 2017.

[140] G. Papadimitriou, A. T. Kruppa, N. Michel, W. Nazarewicz, M. Płoszajczak, and J. Rotureau. Charge radii and neutron correlations in helium halo nuclei. *Phys. Rev. C*, 84:051304, 2011.

[141] I. Sick. Form factors and radii of light nuclei. *J. Phys. Chem. Ref. Data*, 44:031213, 2015.

[142] G. W. Fan, M. Fukuda, D. Nishimura, X. L. Cai, S. Fukuda, I. Hachiuma, C. Ichikawa, T. Izumikawa, M. Kanazawa, A. Kitagawa, T. Kuboki, M. Lantz, M. Mihara, M. Nagashima, K. Namihira, Y. Ohkuma, T. Ohtsubo, Zhongzhou Ren, S. Sato, Z. Q. Sheng, M. Sugiyama, S. Suzuki, T. Suzuki, M. Takechi, T. Yamaguchi, and W. Xu. Density distribution of ^{8}Li and ^{8}B and capture reaction at low energy. *Phys. Rev. C*, 91:014614, 2015.

[143] G.A. Korolev, A.V. Dobrovolsky, A.G. Inglessi, G.D. Alkhazov, P. Egelhof, A. Estradé, I. Dillmann, F. Farinon, H. Geissel, S. Ilieva,

Y. Ke, A.V. Khanzadeev, O.A. Kiselev, J. Kurcewicz, X.C. Le, Yu.A. Litvinov, G.E. Petrov, A. Prochazka, C. Scheidenberger, L.O. Sergeev, H. Simon, M. Takechi, S. Tang, V. Volkov, A.A. Vorobyov, H. Weick, and V.I. Yatsoura. Halo structure of ^{8}B determined from intermediate energy proton elastic scattering in inverse kinematics. *Phys. Lett. B*, 780:200, 2018.

[144] R. Han, J. X. Li, J. M. Yao, J. X. Ji, J. S. Wang, and Q. Hu. Effects of pairing correlations on formation of proton halo in ^{9}C. *Chin. Phys. Lett.*, 27:092101, 2010.

[145] I. J. Thompson and M. V. Zhukov. Effects of ^{10}Li virtual states on the structure of ^{11}Li. *Phys. Rev. C*, 49:1904, 1994.

[146] M. Cavallaro, M. De Napoli, F. Cappuzzello, S. E. A. Orrigo, C. Agodi, M. Bondí, D. Carbone, A. Cunsolo, B. Davids, T. Davinson, A. Foti, N. Galinski, R. Kanungo, H. Lenske, C. Ruiz, and A. Sanetullaev. Investigation of the ^{10}Li shell inversion by neutron continuum transfer reaction. *Phys. Rev. Lett.*, 118:012701, 2017.

[147] A. M. Moro, J. Casal, and M. Gómez-Ramos. Investigating the ^{10}Li continuum through ^{9}Li(d,p)^{10}Li reactions. *Phys. Lett. B*, 793:13, 2019.

[148] F. Barranco, G. Potel, E. Vigezzi, and R. A. Broglia. ^{9}Li(d,p) reaction as a specific probe of ^{10}Li, the paradigm of parity-inverted nuclei around the $N = 6$ closed shell. *Phys. Rev. C*, 101:031305, 2020.

[149] H. G. Bohlen, A. Blazevic, B. Gebauer, W. Von Oertzen, S. Thummerer, R. Kalpakchieva, S.M. Grimes, and T.N. Massey. Spectroscopy of exotic nuclei with multi-nucleon transfer reactions. *Prog. Part. Nucl. Phys.*, 42:17, 1999.

[150] J. K. Smith, T. Baumann, J. Brown, P. A. DeYoung, N. Frank, J. Hinnefeld, Z. Kohley, B. Luther, B. Marks, A. Spyrou, S. L. Stephenson, M. Thoennessen, and S. J. Williams. Selective population of unbound states in ^{10}Li. *Nucl. Phys. A*, 940:235, 2015.

[151] R. Sherr and H. T. Fortune. Energies within the $A = 10$ isospin quintet. *Phys. Rev. C*, 87:054333, 2013.

[152] H. T. Fortune. Mirror energy differences of $2s_{1/2}$ single-particle states: Masses of ^{10}N and ^{13}F. *Phys. Rev. C*, 88:024309, 2013.

[153] J. Hooker, G.V. Rogachev, V.Z. Goldberg, E. Koshchiy, B.T. Roeder, H. Jayatissa, C. Hunt, C. Magana, S. Upadhyayula, E. Uberseder, and A. Saastamoinen. Structure of ^{10}N in ^{9}C+p resonance scattering. *Phys. Lett. B*, 769:62, 2017.

[154] S. M. Wang, W. Nazarewicz, R. J. Charity, and L. G. Sobotka. Structure and decay of the extremely proton-rich nuclei ^{11,12}O. *Phys. Rev. C*, 99:054302, 2019.

[155] D.R. Tilley, J.H. Kelley, J.L. Godwin, D.J. Millener, J.E. Purcell, C.G. Sheu, and H.R. Weller. Energy levels of light nuclei A=8,9,10. *Nucl. Phys. A*, 745:155, 2004.

[156] S. Aoyama, K. Katō, and K. Ikeda. Resonant structures in the mirror nuclei ^{10}N and ^{10}Li. *Phys. Lett. B*, 414:13, 1997.

[157] A. Lépine-Szily, J. M. Oliveira, V. R. Vanin, A. N. Ostrowski, R. Lichtenthäler, A. Di Pietro, V. Guimarães, A. M. Laird, L. Maunoury, G. F. Lima, F. de Oliveira Santos, P. Roussel-Chomaz, H. Savajols, W. Trinder, A. C. C. Villari, and A. de Vismes. Observation of the particle-unstable nucleus ^{10}N. *Phys. Rev. C*, 65:054318, 2002.